Chapter 4

Experimental studies on a binary mixture exhibiting a new type of Nematic-Nematic transition

4.1   Introduction

In the previous chapter we described the pressure-temperature phase diagram of a pure nematogen exhibiting the N_1N_d transition. We also studied binary mixtures of two highly polar compounds with the intention of getting the N_1N_d transition temperature to lie above the ambient at atmospheric pressure. In this chapter, we present detailed studies on a different binary mixture. Though we do observe a nematic-nematic transition in these mixtures, we have experimental evidence to show that it does not correspond to the N_1N_d transition. It is indeed a new type of nematic-nematic transition. We have carried out X-ray diffraction studies on one of the binary mixtures and found that the measured layer spacing d of short range ordered groups corresponds to a partial bilayer structure and remains a constant throughout the nematic range (see section 4.33). In view of this result we call this new type of NN transition as N_lN_h transition associated with a change in the concentrations of different types of short range ordered groups of molecules, all with antiparallel association (see section 4.5). The symbol N_l represents the nematic phase at low temperatures and N_h, the nematic phase at high temperatures. We have carried out optical path difference measurements on various compositions of this binary mixture contained in planar aligned cells. The N_lN_h transition temperature decreases with increasing thickness of the cell in *planar* aligned samples. We show that the birefringence $\Delta\mu$, which is a measure of the orientational order parameter S, is enhanced in *planar* aligned *thin* cells compared to that measured in thick cells. We have also carried out light scattering experiments on homeotropically aligned samples observed between crossed polarisers. The intensity of light scattered by the sample is monitored in a narrow range of angles near the forward direction. The N_lN_h transition shows up as a peak in the scattered intensity. In this geometry, the transition temperature is found to be independent of cell thickness. We have also observed a substantial slowing down of director fluctuations near the N_lN_h transition point indicating that it is close to a critical point. We have also measured the dielectric constant $\varepsilon_{\parallel}$ using the

homeotropically aligned cells which however did not show any signature of this transition. The measurements of relaxation frequency (see section 4.312) indicate that the strength of nematic potential felt by the molecule with longer aromatic core is lower at higher temperatures than that at lower temperatures indicating a change in short range order in the medium.

4.2   Experimental

A few binary mixtures of CP6B and 4PCPP of different compositions are used in the experimental studies to be reported in this chapter. The chemical structures and the transition temperatures of the compounds used are shown in Figure 4.1.
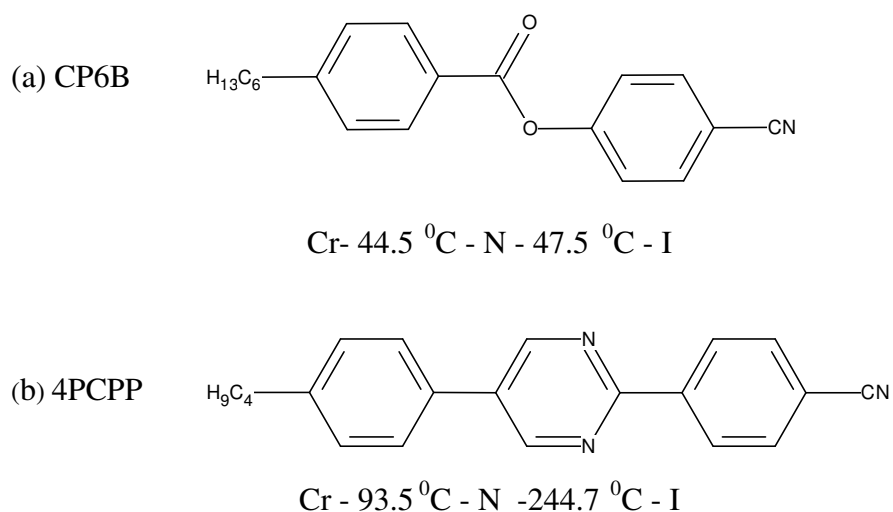
(a) CP6B

$$Cr- 44.5 \ ^0C - N - 47.5 \ ^0C - I$$

(b) 4PCPP

$$Cr - 93.5 \ ^0C - N \ -244.7 \ ^0C - I$$

Figure 4.1: Chemical Structures and transition temperatures of CP6B and 4PCPP.

4.21 Measurement of scattered intensity from homeotropically aligned cells

We have prepared homeotropically aligned samples using the following method. The ITO coated glass plates are treated with octadecyl triethoxy silane (ODSE), and are cured for about an hour at 150 ^{0}C. ODSE is a long chained amphiphilic molecule. The polar end group is attracted to the surface of the glass plate and the long aliphatic chain interacts with the alkyl chain of the liquid crystal giving rise to perpendicular orientation of the director with respect to the glass plate. The cells are prepared using ODSE coated glass plates adopting the procedure explained in Chapter 3 (see section 3.2). The thickness of the cell is measured using an Ocean

Optics spectrometer and cells of uniform thickness are chosen for experiments. The sample is filled into the cell in the isotropic phase through capillary action.
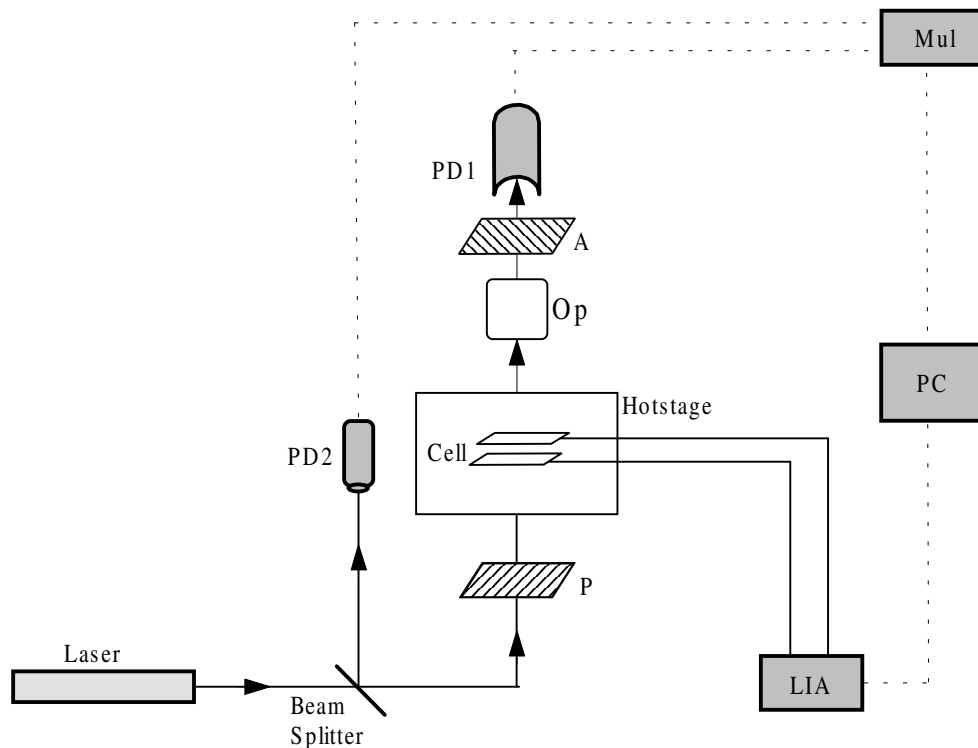

Figure 4.2: Schematic representation of the experimental setup to measure the scattered intensity. P - polariser, A - Analyser, Op - optics of the microscope, PD1, PD2 - photodiodes, Mul- multimeter, LIA- lock-in-amplifier.
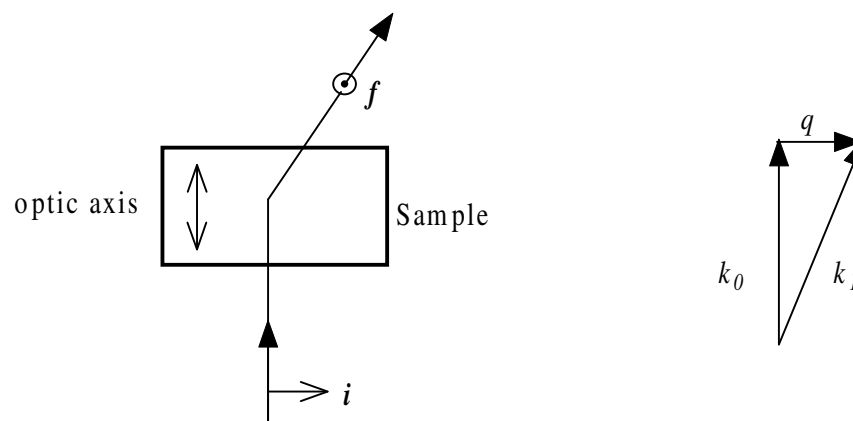

Figure 4.3: Schematic representation of the scattering geometry [1]. i and f represent the polarization vectors of the incident and scattered beams. The wave vectors of the incident beam and the scattered beam are denoted by k_0 and k_1 respectively. q is the scattering vector.

A schematic diagram of the experimental setup used to measure the intensity of light scattering from a homeotropically aligned sample is shown in Figure 4.2. The sample is mounted in a hot-stage (Instec, HS1). The temperature of the hot-stage is controlled using the MK1 software to an accuracy of 10mK. The hot-stage is placed on the rotating stage of a microscope (Leitz, Orthoplan) between crossed polarisers. A He-Ne laser beam (Oriel; 3mW) of 633nm is split into two beams. One of the beams passes through the sample placed between crossed polarisers. The transmitted intensity is zero in this geometry as the incident beam is along the optic axis of the sample. However, due to thermal fluctuations of the director $\hat{n}$ there will be strong scattering of light.

A schematic representation of the scattering geometry is shown in Figure 4.3. The propagation direction of the incident wave vector k_0 is along the optic axis $\hat{n}$ of the nematic sample. The directions of electric vectors of the incident beam and the scattered beam are denoted by i and f (Figure 4.3).

In this geometry the scattered intensity I [1] will be given by

$$I \propto \frac{\varepsilon_{ai}^2}{\left(K_{33}q_{\parallel}^2 + K_{22}q_{\perp}^2\right)} \qquad 4.1$$

where K_{33} and K_{22} are bend and twist elastic constants respectively and ε_{ai} is the anisotropy of optical susceptibility.

For $\vec{q} = \vec{k}_0 - \vec{k}_1 \approx 0$, the scattered intensity is large (equation 4.1). We have conducted measurements on the samples in the orthoscopic configuration of the microscope (parallel beam observation). For $\vec{k}_0 \approx \vec{k}_1$ the scattered intensity is given by $I \propto \frac{\varepsilon_{ai}^2}{\left(K_{22}q_{\perp}^2\right)}$. The scattered intensity in the forward direction in a narrow range of angles with $\vec{q} \approx 0$ is detected using a photo-detector (PD1: INTEVAC intensified photodiode with a relatively large cathode area ~ 0.5 cm^2). The stability of the laser beam is monitored using a photodiode (PD2: Centronics model OSD-5). The outputs of the photodiodes are measured using a multimeter (MUL: Keithley multimeter model 2000). The scattered intensity is recorded using an automated program at

temperature steps of 0.2 ^{0}C or 0.5 ^{0}C from isotropic phase down to the required temperature.

4.22   Dielectric constant measurements

We have carried out measurements of dielectric constants of some samples as functions of temperature. The dielectric measurements were conducted using a simple technique developed by Basappa et al [2] and is described below. Normally ionic impurities are present in liquid crystal samples which contribute to a finite resistance of the sample cell. The equivalent electrical circuit of a liquid crystal cell is considered to be a capacitance (C_S) in parallel with a resistance (R_S). A schematic representation of the experimental setup used is shown in Figure 4.4. A lock-in amplifier (LIA:SRS model 830) is used to apply an electric field to the sample for conducting dielectric measurements.
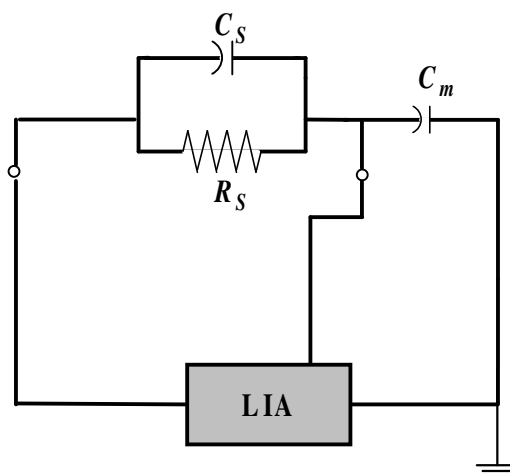

Figure 4.4: Equivalent circuit used for the impedance analysis of the liquid crystal cell. C_S and R_S are the sample capacitance and resistance respectively.

We measure the amplitude and phase of the voltage developed across a series capacitance, C_m (= 1 μF) which is large in comparison to the sample capacitance C_S (~150 pF). A large value of capacitance C_m is chosen so that the maximum voltage drop is across the cell and only a small voltage is measured by the lock-in amplifier.

The impedance of the modeled sample cell is given by

$$Z_s = R_s \frac{(1 - i\omega C_s R_s)}{(1 + \omega^2 C_s^2 R_s^2)} \qquad 4.2$$

where R_S and C_S are the sample resistance and capacitance respectively. $\omega = 2\pi f$ where f is the frequency of the applied voltage and $i = \sqrt{-1}$. The total impedance of the circuit Z_t, which is a series combination of Z_s and $Z_m = 1/i\omega C_m$ is given by

$$Z_t = \frac{\omega R_s C_m - i\left[1 + \omega^2 R_s^2 C_s (C_m + C_s)\right]}{\omega C_m (1 + \omega^2 C_s^2 R_s^2)} \qquad 4.3$$

The total current flowing through the circuit is given by

$$I_t = \frac{V_0 e^{i(\omega t + \phi_0)}}{Z_t} \qquad 4.4$$

where V_0 and ϕ_0 are the amplitude and phase of the output voltage of the LIA.

Substituting Z_t in equation 4.3 we get

$$I_t = \frac{V_0 e^{i(\omega t + \phi_0)} \omega C_m (1 + \omega^2 C_s^2 R_s^2)}{\omega R_s C_m - i\left[1 + \omega^2 R_s^2 C_s (C_m + C_s)\right]} \qquad 4.5$$

The voltage drop measured across C_m is given by

$$V_m e^{i(\omega t + \varphi_m)} = I_t Z_m \qquad 4.6$$

where V_m and φ_m are the amplitude and phase of the measured signal. The above expression is simplified by separating the real and imaginary parts and we get the following relations for the resistance and capacitance of the sample [2]

$$R_s = \frac{Y}{\omega \sin \gamma} \qquad 4.7$$

$$C_s = \frac{X}{Y} \qquad 4.8$$

where $X = \cos\gamma - Q$, $Y = \dfrac{\sin^2 \gamma + X^2}{C_m Q}$, $Q = \dfrac{V_m}{V_0}$ and $\gamma = \phi_0 - \phi_m$. Using standard capacitors in parallel with standard resistors in place of the liquid crystal cell the setup was calibrated. We found that the stray capacitance is ~2 pF. The measurements were carried out by a computer using a suitable program. The accuracy of the

measured capacitance is ~1% and that of the resistance is ~3%. The capacitance of the empty cell (C_0) is measured before filling liquid crystal sample. The ratio of the capacitance of the sample (C_s) to the empty cell capacitance (C_0) gives the dielectric constant ε of the sample.

4.23 Optical path difference measurements on planar aligned samples

The birefringence $\Delta\mu$ of *planar* aligned thick samples are measured as explained in Chapter 3 (see section 3.2). The intensity data at I_{max} and I_{min} of the corresponding branch in the intensity profile are needed to estimate the value of $\Delta\mu$ (see section 2.29). But in thin cells the transmitted intensity profile does not show a maximum and a minimum. Hence a quarter wave plate compensator is used to measure the optical phase difference of thin samples.
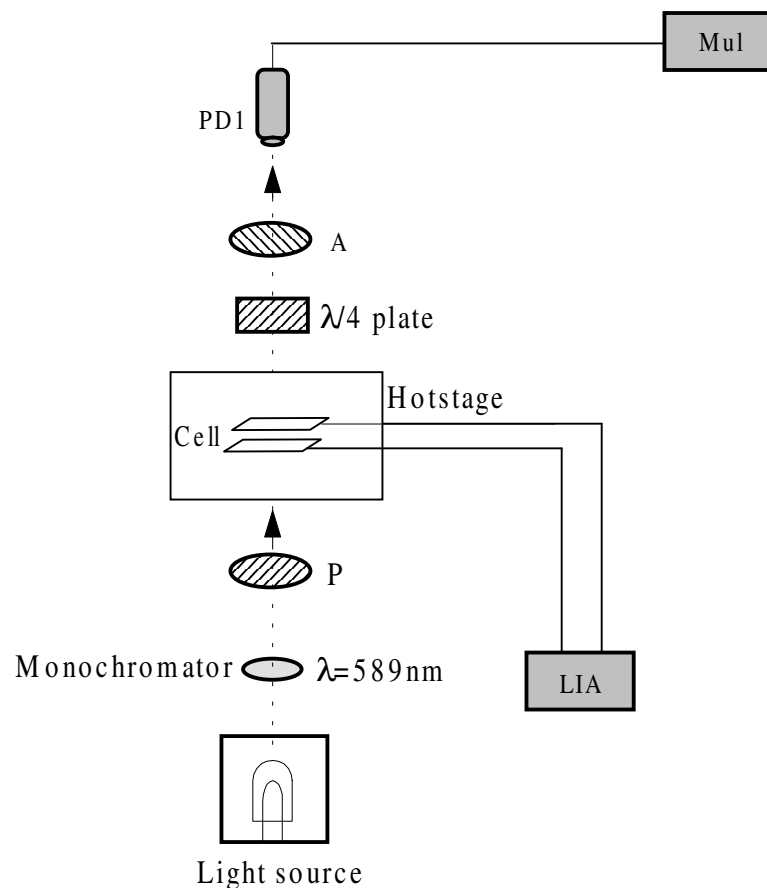

Figure 4.5: Schematic diagram of experimental setup used to measure the optical path difference of sample. LIA - lock-in amplifier, PD1 - photo diode.

A schematic diagram of the setup used in the optical phase difference measurement of thin cells is shown in Figure 4.5. Initially the polariser and analyser of the microscope are set at 0^0 and 90^0 respectively. The sample in the nematic phase between crossed polarisers is rotated to locate the orientation of minimum intensity. In this orientation the director $\hat{n}$ determined by the rubbing direction of the sample will be parallel to one of the crossed polarisers. An interference filter is used to get a beam in a narrow band around λ=589nm. A quarter wave (λ/4) plate is introduced in the slot provided in the microscope between the sample and the analyser. The slow axis of the λ/4 plate is fixed at 45^0 with respect to horizontal polarisation. Both polariser and analyser in tandem are rotated by 45^0 from the initial crossed orientation. This ensures that the electric vector of the light entering the sample is at an angle of 45^0 to the principal axes of the sample and the principal axes of the quarter wave plate are at 45^0 to those of the sample.

When the polarised light beam passes through a birefringent liquid crystal whose principal axes are at 45^0 to the electric vector of the light beam, the emergent beam consists of two linearly polarised components of equal amplitudes, one component being phase shifted by $2\pi t\Delta\mu/\lambda$ with respect to the other, where λ is the wavelength of incident beam. When these two orthogonal components pass through a quarter wave plate arranged as described above, they are converted into two circularly polarized beams of opposite sense. Superposition of these beams yields a linearly polarised light beam with its direction of vibration rotated by $\pi t\Delta\mu/\lambda$ with respect to the direction of vibration of the light beam incident on the liquid crystal sample. The analyser is rotated by an angle ϑ to get the minimum intensity. This angle ϑ is a measure of the optical phase difference and is given by $\vartheta = \pi t\Delta\mu/\lambda$. The absolute value of optical phase difference is again determined using Freedericks transition technique (see section 1.25, chapter 1).

4.3   Results

4.31   Measurements on homeotropically aligned cells

4.311   Light scattering experiments

We have carried out scattered intensity measurements on binary mixtures of CP6B with 4PCPP. The measurements were made on samples with seven different concentrations of CP6B and the data are presented in Figures 4.6 to 4.12. In all the mixtures a strong enhancement in scattering is seen at the temperatures corresponding to the NI transition. A second enhancement in the scattered intensity is seen at lower temperatures, corresponding to the N_lN_h transition and the temperature at which the peak is observed is considered to be the N_lN_h transition temperature. As mentioned in section 3.1 the curvature elastic constant K is expected to reduce drastically near the N_lN_h transition, hence a peak in the scattered intensity can be expected at this transition, as the scattering intensity is $\propto 1/K_{22}q^2$ [1]. Far away from these transitions the back ground intensity is relatively small as the elastic constant K has values of a typical nematic. In well aligned samples the background intensity increases with increasing thickness of the sample as the sample volume scattering the light beam increases. The background intensity is relatively large in some samples (see Figures 4.9, 4.10b and 4.12b) due to the presence of some defects in the alignment of the sample. The alignment of different cells were not of the same quality as they were prepared in different batches. In the cell of 7.2 μm thickness (Figure 4.10b) for a mixture with 58 mol% of CP6B, the background intensity is high and noisy. Nevertheless a large peak corresponding to N_lN_h transition is clearly noticeable. The background intensity in the lower temperature N_l phase is higher compared to that measured in the higher temperature N_h phase. In all the cells with good alignment the temperature range for which an enhancement in scattered intensity is observed is ~ 6 - 7 ^{0}C.
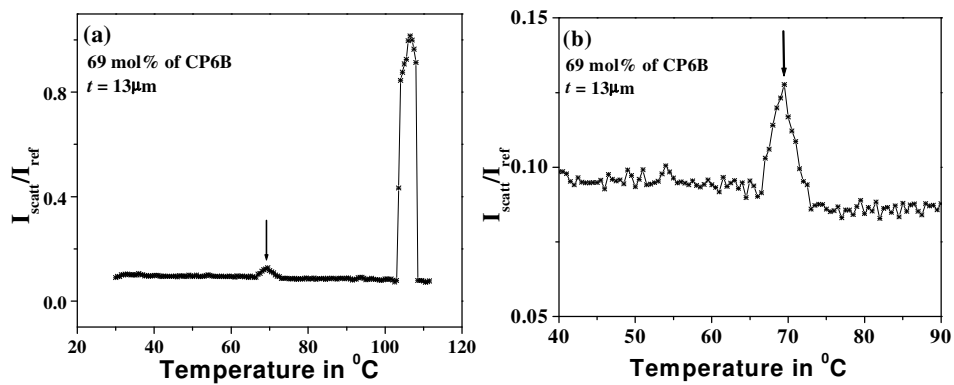
Figure 4.6: The variation of the ratio of scattered intensity to reference intensity as a function of temperature in a cell of thickness $t = 13$ μm of a binary mixture with 69 mol% of CP6B (a) over the entire nematic range, (b) on an expanded scale around the N_lN_h transition. The N_lN_h transition is indicated by arrows.
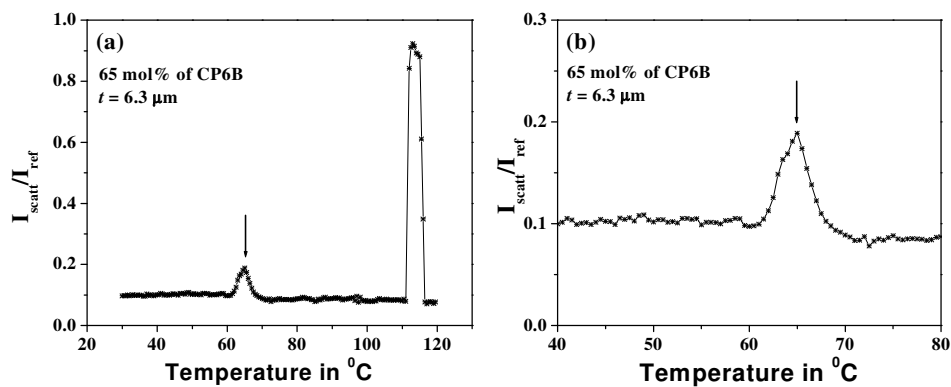

Figure 4.7: Scattered intensity profile for a mixture with 65 mol% of CP6B in a cell of thickness $t = 6.3$ μm. (a) over the entire nematic range, (b) on an expanded scale around the N_lN_h transition.
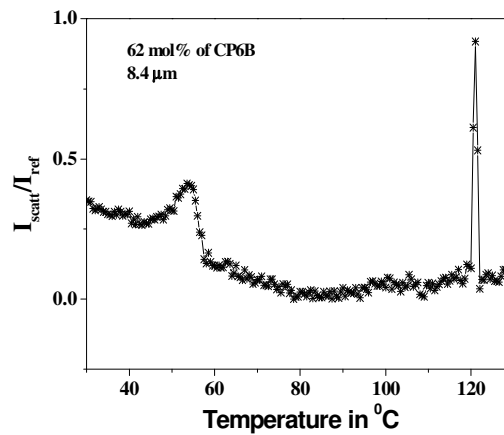
Figure 4.8: The temperature variation of the ratio of scattered intensity to reference intensity for a mixture with 62 mol% of CP6B in a cell of thickness 8.4 μm.
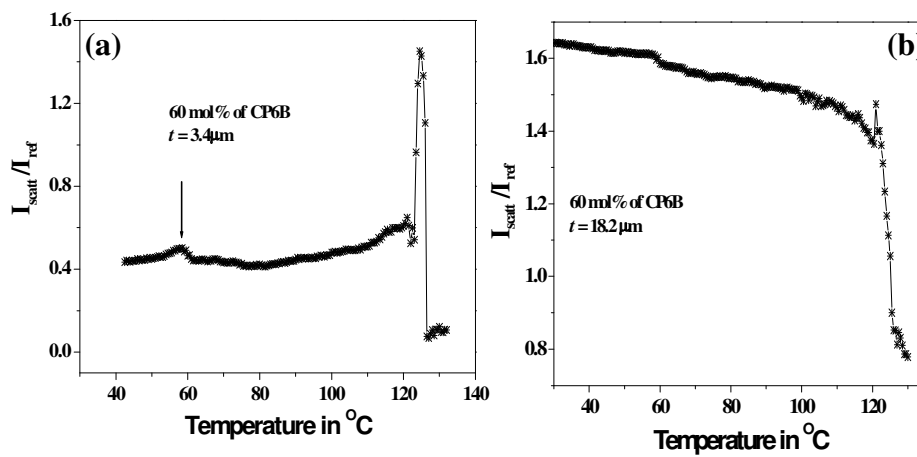

Figure 4.9: The variation of the ratio of scattered intensity to reference intensity as a function of temperature for a mixture with 60 mol% of CP6B in cells of thicknesses (a) $t = 3.4$ μm (b) $t = 18.2$ μm.
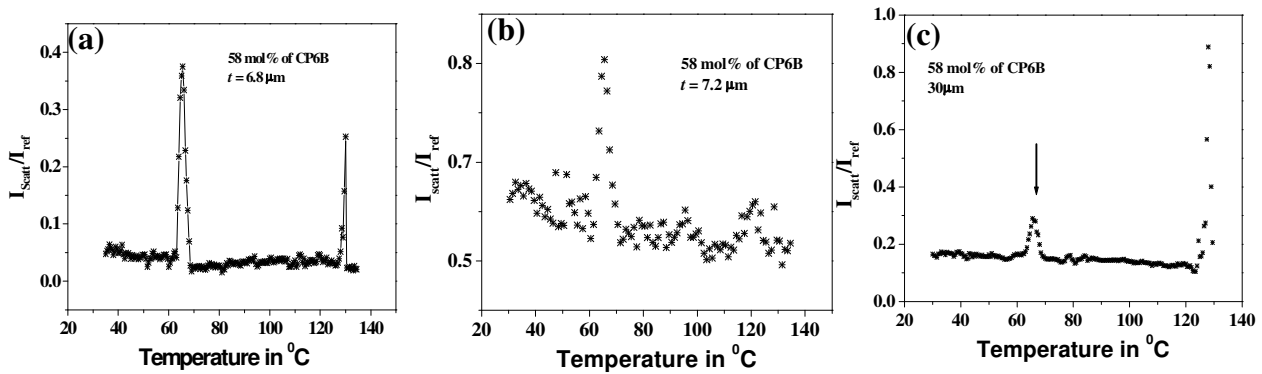
Figure 4.10: The variation of the ratio of scattered intensity to reference intensity as a function of temperature for a mixture with 58 mol% of CP6B in cells of thicknesses (a) $t = 6.8$ µm (b) $t = 7.2$ µm and (c) $t = 30$ µm.
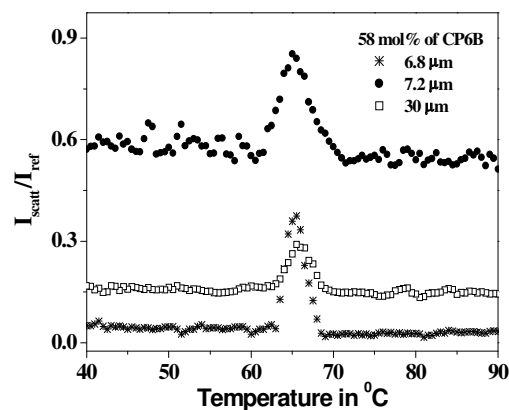

Figure 4.11: The variation of the ratio of scattered intensity to reference intensity as a function of temperature for a mixture with 58 mol% of CP6B in cells of thicknesses 6.8 µm , 7.2 µm and 30 µm on an expanded scale around the $N_l N_h$ transition.

In Figure 4.10 data of three different cell thicknesses for a mixture with 58 mol% of CP6B are shown. In Figure 4.11 we have plotted all the data for the three cells together on an expanded scale in a temperature range around $N_l N_h$ transition. It can be noticed that the peaks for all the three cells are observed at the same temperature of   ~65 ^{0}C. This indicates that the $N_l N_h$ transition temperature is independent of the cell thickness in this geometry.
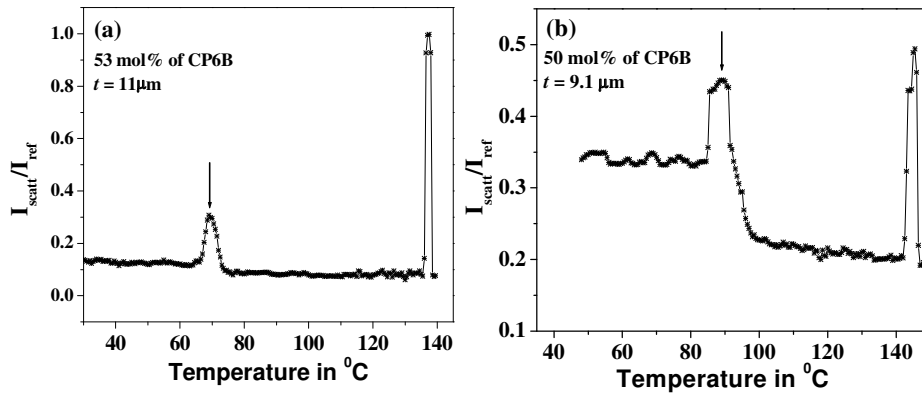
Figure 4.12: The variation of the ratio of scattered intensity to reference intensity as a function of temperature in (a) 11 μm thick cell for a mixture with 53 mol% of CP6B (b) 9.1 μm thick cell for a mixture with 50 mol% of CP6B.
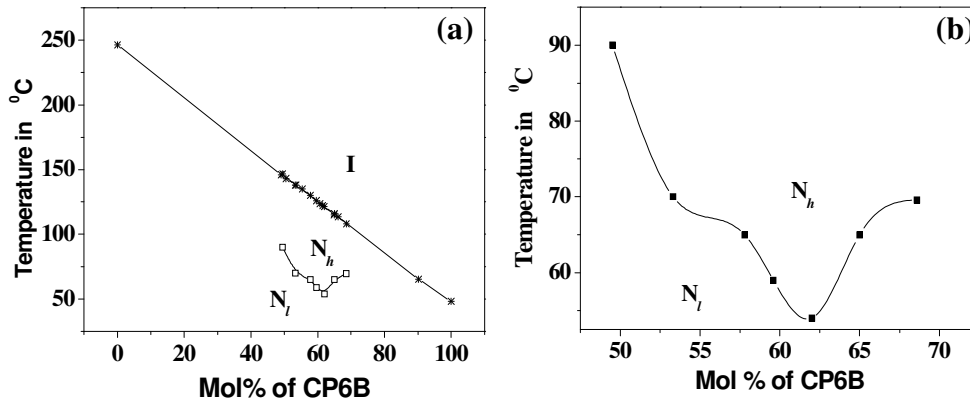

Figure 4.13: The concentration-temperature phase diagram of binary mixture of CP6B and 4PCPP constructed using the scattered intensity data from homeotropically aligned cells.

We have constructed the concentration-temperature phase diagram (Figure 4.13) using the data from Figures 4.6 - 4.12. In Figure 4.13a both NI and N_lN_h transitions are shown. In Figure 4.13b only N_lN_h transition temperatures are plotted on an expanded temperature scale for clarity. The N_lN_h transition temperature has a minimum value for a mixture with 62 mol% concentration of CP6B and increases on either side of this concentration, whereas the NI transition temperature linearly decreases with increasing concentration of CP6B. We will compare this phase diagram with the one constructed using planar aligned cells in the next section (see section 4.32).

On careful visual observation of the sample using white light the scattering of the light due to thermal fluctuations of the director can be seen at all temperatures and is relatively weak. But in a narrow range of temperatures around the N_lN_h transition point we could observe that the sample was brightening and darkening over a fairly long time with an interval of ~ 30-60 seconds in *all* the samples. The director response time of the nematic medium is $\Gamma = \eta t^2/\pi^2 K$ where K is the effective curvature elastic constant, η is the effective viscosity of the nematic medium [1]. For a typical nematic liquid crystal $K\sim10^{-6}$ dynes, $\eta \sim 0.1$ poise, the value of $\Gamma \sim 2.5$ ms for a cell of thickness $t = 5$ μm. The long lived brightening and darkening of the sample observed in a narrow range of temperature around the N_lN_h transition point indicates that there is a critical slowing down of the director fluctuations.

We have monitored the scattered intensity using a laser beam adopting the experimental method described in section 4.21 as a function of <u>time</u> at different constant temperatures. We have used a mixture with 60 mol% of CP6B taken in a cell of thickness 5.2 μm and recorded the scattered intensity data as a function of time at a few temperatures on cooling the sample from 76 ^{0}C to 44 ^{0}C. We have monitored the intensity in 4000 steps at sampling intervals of $t_s = 0.175$ seconds. The data at three different temperatures are presented in Figures 4.14 and 4.15. As t_s is larger by about two orders of magnitude than the value of Γ estimated above, the response of director taking place within the time Γ is not accessible. Far away from N_lN_h transition the temporal variation of the scattered intensity appears as a noise. The data at a temperature of 67 ^{0}C is shown in Figure 4.14a. At any given temperature in the range of ~ 65 to 59 ^{0}C the scattered intensity shows large peaks of different heights at irregular intervals of time. The data at a temperature of 61.2 ^{0}C is shown in Figure 4.15. It shows that there are long lived large fluctuations as already mentioned. This indicates that there is a critical slowing down of the director fluctuations and the N_lN_h transition temperatures in mixtures of all the above compositions are close to the critical point. Again at temperatures below ~ 59 ^{0}C, the data is noisy as shown in Figure 4.14b.

Figure 4.14: The variation of ratio of scattered intensity to reference intensity from a 5.2 μm cell containing a mixture with 60 mol% of CP6B as a function of time at (a) 67 ^{0}C and (b) 58 ^{0}C.

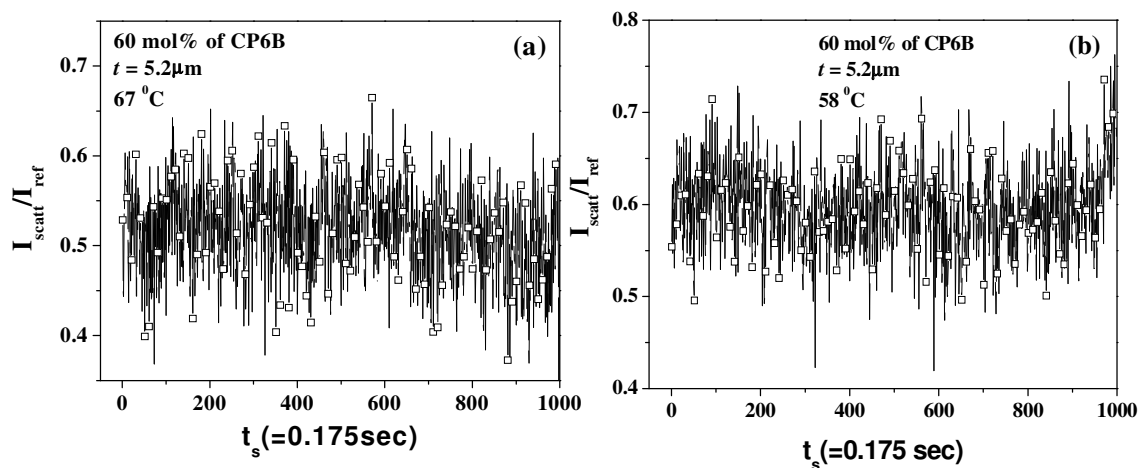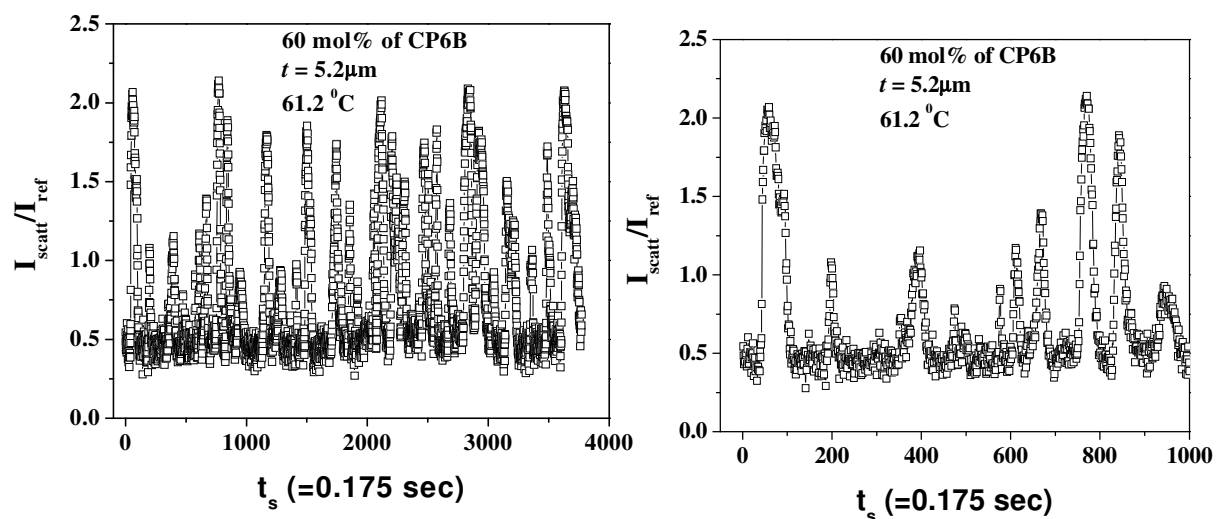
Figure 4.15: The variation of ratio of scattered intensity to reference intensity from a 5.2 μm cell containing a mixture with 60 mol% of CP6B as a function of time at 61.2 ^{0}C (a) over 4000 steps i.e. ~ 700 seconds (b) on an expanded time scale upto 1000 steps.

A temporal correlation function measures the degree to which two dynamical properties are correlated over a period of time. The intensity autocorrelation function $<I(t)I(t+\tau)>$ is a measure of the autocorrelation between two values of intensities, $I(t)$ and $I(t+\tau)$ at times t and $t+\tau$, where τ is the time step at which the data are correlated. We have calculated the intensity autocorrelation function at different temperatures using the scattered intensity data recorded as function of time at those temperatures. The results for two different temperatures close to the N_lN_h transition are shown in Figure 4.16. In both the figures the initial decay occurs within a few seconds indicating that there is a strong correlation within that time. In Figure 4.16a apart from the initial decay, two strong peaks with $\gtrsim 10\%$ increase above background can also be seen at $\tau = 62$ and 125 seconds. Similarly in Figure 4.16b at a temperature of $61.8\,^0C$ there are two strong peaks at $\tau = 67$ and 134 seconds. The experimental setup was placed on an ordinary table which is not vibration free. It is possible that some noise signal is being picked up and getting amplified due to the large sensitivity of the system near the critical region giving rise to the peaks.
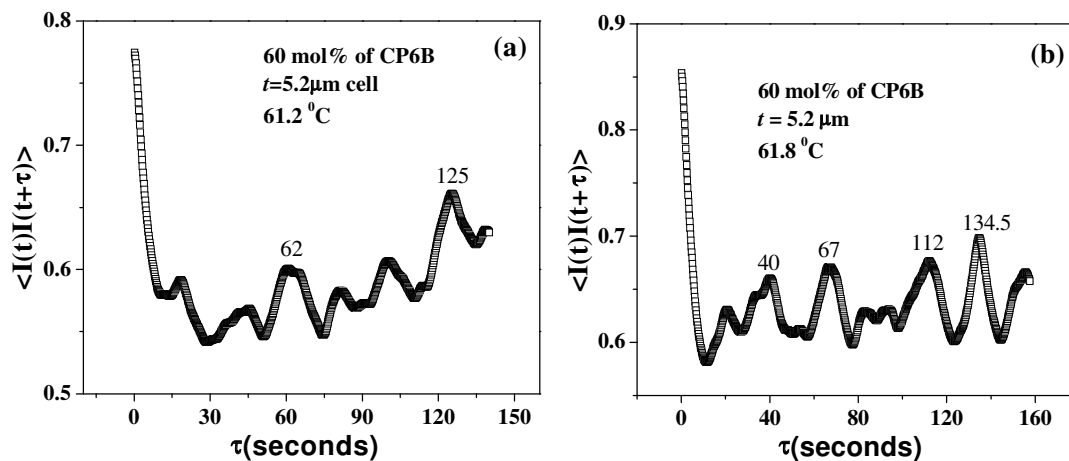
Figure 4.16: The variation of intensity autocorrelation function as a function of time at temperatures (a) $61.2\,^0C$ and (b) $61.8\,^0C$.

The $<I(t)I(t+\tau)>$ data points within the initial decay time are fitted to an exponential function of the form $y=y_0+A_1e^{-(\tau/\tau_0)}$, where y_0, A_1 and τ_0 (the relaxation time) are the fit parameters. One such fitting of the data at a temperature of $63.2\,^0C$ is presented in the Figure 4.17.

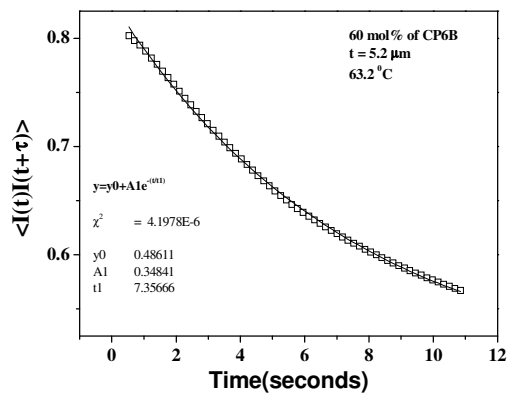Figure 4.17: The variation of intensity autocorrelation $<I(t)I(t+\tau)>$ (within the initial decay) as a function of time at 63.2 ^{0}C. The open squares correspond to experimental data and the solid line is obtained by fitting to an exponential function.
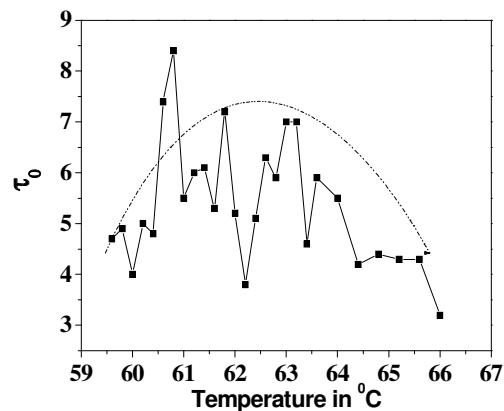
Figure 4.18: The variation of relaxation time τ_0 as a function of temperature.

We have plotted the relaxation time τ_0 as a function of temperature in Figure 4.18, in which a few peaks are seen. As the measurements were not conducted in a vibration free environment, due to the large sensitivity in the critical region a broad transition is indicated as shown by a smooth dashed curve. Another possibility is that more than one NN transition as theoretically predicted by Prost et al [3] may be taking place. Detailed experimental investigations in a vibration free experimental condition are needed to clarify this point.

4.312 Dielectric measurements

The impedance measurements on homeotropically aligned samples are carried out using the method described in section 4.2. The measurements were carried out at a frequency of 4.11kHz and the applied voltage was ~ 2V. To verify the calibration of the system we have measured the dielectric constant $\varepsilon_{\parallel}$ of the pure CP6B using a cell of 7.1 μm thickness. The temperature variation of $\varepsilon_{\parallel}$ is presented in Figure 4.19, and is in good agreement with the one measured by Titov et al [4].
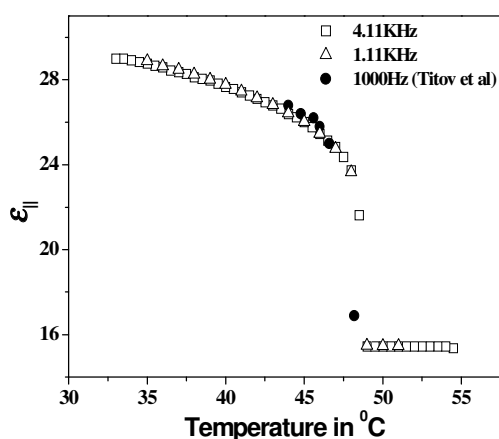

Figure 4.19: Temperature variation of the dielectric constant $\varepsilon_{\parallel}$ of CP6B measured in a cell of thickness 7.1μm. The data of Titov et al [4] are also shown.
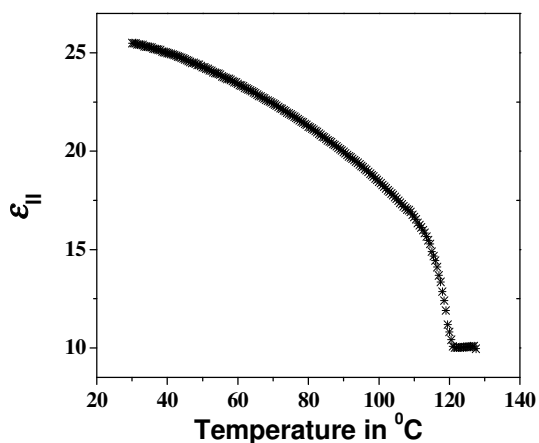

Figure 4.20: Temperature variation of the dielectric constant $\varepsilon_{\parallel}$ measured for a binary mixture with 62 mol% of CP6B in a 8.4 μm thick cell.

The temperature variation of $\varepsilon_{\parallel}$ estimated using the capacitance data for a binary mixture with 62 mol% of CP6B in a 8.4μm thick cell is shown in Figure 4.20. In Figure 4.8 the scattered intensity data on the same cell is given in which there is a clear indication of $N_l N_h$ transition at about 54 ^{0}C. However, we could not detect any signature of this transition in the dielectric constant. The dielectric constant $\varepsilon_{\parallel}$ is given by $\varepsilon_{\parallel} = \bar{\varepsilon} + \frac{2}{3}\Delta\varepsilon_0 S$, where S is the orientational order parameter, $\bar{\varepsilon} = (\varepsilon_{\parallel} + 2\varepsilon_{\perp})/3$ is the average dielectric constant and $\Delta\varepsilon_0$ is the value of dielectric anisotropy $(\varepsilon_{\parallel} - \varepsilon_{\perp})$ in the fully aligned state. A typical jump in the order parameter S at the $N_l N_h$ transition is ~1% (see section 4.32). In mesogens with highly polar end groups $\varepsilon_{\parallel}$ is $\propto S/T$ (see section 1.23). Hence the expected jump in $\varepsilon_{\parallel}$ at the $N_l N_h$ transition is also ~1% and is not detected in our measurements. In Figure 4.21 we present the data on mixtures with 60 mol% of CP6B and 58 mol% of CP6B. The absence of a slope change in $\varepsilon_{\parallel}$ near the $N_l N_h$ transition also indicates that the short range order below the transition temperature may not be of the N_1 type with a polar character.
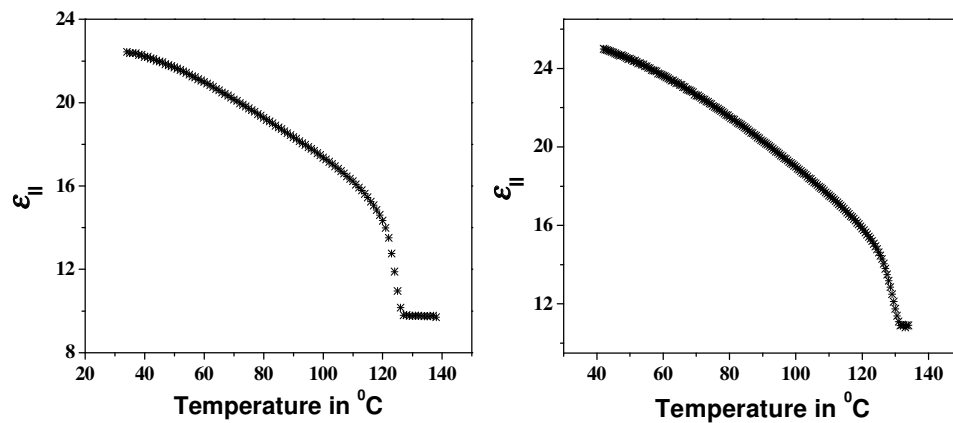

Figure 4.21: Temperature variation of the dielectric constant $\varepsilon_{\parallel}$ for binary mixtures (a) with 60 mol% of CP6B a in a 5.2 μm thick cell, (b) with 58 mol% of CP6B in a cell of thickness 6.8 μm.

The variations of $\varepsilon_\parallel$ for binary mixtures with four different concentrations viz. 65, 62, 60 and 58 mol% of CP6B are shown as functions of temperature in Figure 4.22a. The $\varepsilon_\parallel$ at a given relative temperature of $T_{NI} - T$, has a minimum value for a mixture with 60 mol% of CP6B and on either side of this concentration the value of $\varepsilon_\parallel$ increases as shown in Figure 4.22b. In the concentration - temperature phase diagram also a similar behaviour is observed for the N_lN_h transition but the minimum occurs for a binary mixture with 62 mol% of CP6B (see Figure 4.13).
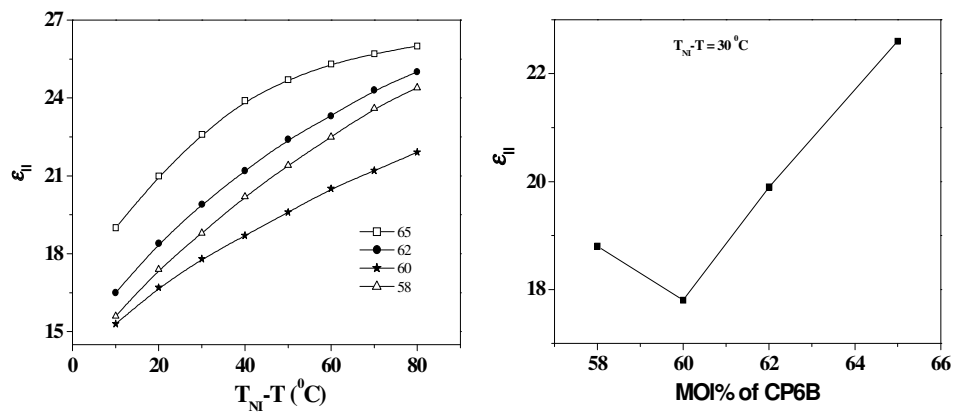

Figure 4.22: (a) Temperature variations of the dielectric constant $\varepsilon_\parallel$ for binary mixtures with four different concentrations of CP6B (b) the variation of the dielectric constant $\varepsilon_\parallel$ of binary mixtures as a function of concentration of CP6B at T_{NI}-T=30 ^{0}C.

It is well known that the dielectric constants are frequency dependent. In the nematic phase the relaxation of $\varepsilon_\perp$ corresponds to the molecular reorientation about the long molecular axis and occurs in the GHz region. The relaxation of $\varepsilon_\parallel$ corresponds to the molecular reorientation about the short molecular axis. This relaxation process is retarded by the nematic potential. Hence the relaxation of $\varepsilon_\parallel$ occurs at very low frequency (MHz or even kHz region). We have carried out the measurements of $\varepsilon_\parallel$ as a function of frequency at various temperatures for a mixture with 58 mol% of CP6B in a cell of thickness t = 6.8 μm. The measurements have been carried out only upto a frequency of 100 kHz which is the maximum frequency accessible using the lock-in amplifier (SRS model 830) . The imaginary part of the

complex dielectric constant ε'' (the dielectric loss) is proportional to the effective conductivity σ of the sample [5]: $\sigma = \omega \varepsilon'' / 4\pi$, where $\omega = 2\pi f$ and f the frequency of applied electric field. We have estimated $\varepsilon''_{||}$ as a function frequency at various temperatures and the results are shown in Figure 4.23. The effect of ionic impurities in the sample is dominant at low frequencies. Confining our attention to the higher frequency data, at any given temperature the frequency at which a peak is observed is considered to be the relaxation frequency f_R. The frequency dependent dielectric loss at different temperatures are shown in Figure 4.23a.

The Cole-Cole plot (plot of $\varepsilon''_{||}$ as a function of $\varepsilon_{||}$) at a few different temperatures are shown in Figure 4.23b. As the data is restricted only upto ~100 kHz we do not attempt to fit the points to a semicircle.
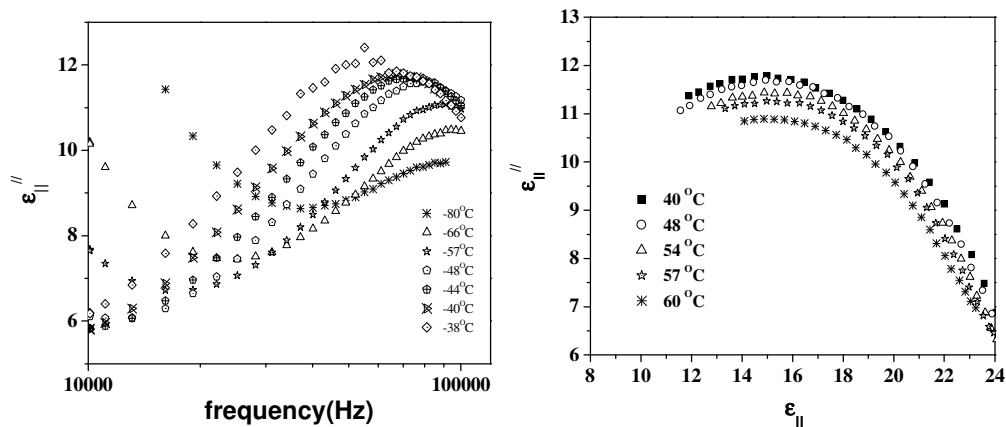
Figure 4.23: (a) The variation of the dielectric loss (imaginary part of the dielectric constant) $\varepsilon''_{||}$ as a function of applied frequency (plotted in a logarithmic scale), (b) Cole-Cole plot for relaxation of $\varepsilon_{||}$, at various temperatures in the nematic range for a mixture with 58 mol% of CP6B in a cell of thickness 6.8 μm.

The relaxation frequency of this system in the temperature range of ~ 38 – 72 ^{0}C occurs in the frequency range ~ 60 – 100 kHz. These values are lower by an order of magnitude compared to that of a typical mesogen like pentyl cyanobiphenyl (5CB), which has $f_R \gtrsim 2$MHz [6]. The binary mixture consists of two

aromatic compounds; viz., CP6B with two aromatic rings and 4PCPP with three aromatic rings (see Figure 4.1). The observed relaxation frequency probably corresponds to that of molecule with longer aromatic core, 4PCPP. Kresse [7] has reported that in a binary mixture consisting of components with two aromatic compounds the relaxation frequency decreases by a decade on lengthening the solute by one phenyl ring.

The relaxation time τ_R decreases as the temperature increases. Meier and Saupe and later Martin et al [8] extended the Debye model of dielectric relaxation in liquids to nematics. They defined a retardation factor $g = \tau_R/\tau_D$, where τ_R is the observed relaxation time of $\varepsilon_\parallel$ in the nematic phase and τ_D, the ordinary Debye relaxation time in the isotropic phase. Assuming that the molecule has only a longitudinal component of dipole moment, the retardation factor g in terms of nematic potential w can be written as

$$g = (k_B T/w) \, [exp(w/k_B T) - 1] \approx (k_B T/w)[exp(w/k_B T)] \qquad 4.9$$

where k_B is the Boltzmann constant.

In the isotropic phase, the hindrance to the molecular reorientation is mainly due to the viscosity of the medium. The temperature dependence of the viscosity [9] is given by $\eta \propto \eta_0 \, exp[w_{vis}/k_B T]$, where w_{vis} is the activation energy due to the viscosity effects and in the isotropic phase $\tau_D = 4\pi\eta a^3/k_B T$, where a is the effective molecular radius. As $\tau_R = g\tau_D$, $\tau_R \propto exp \, [(w+w_{vis})/k_B T]$.

Using this Arrhenius type equation for the relaxation time, we write

$$\tau_R = A \, exp(E_a/k_B T) \qquad 4.10$$

where $E_a = w+w_{vis}$ is the total activation energy for the dielectric relaxation and $A \simeq 4\pi\eta_0 \, a^3/w$.

As $\tau_R = 1/2\pi f_R$, the equation 4.10 can be written as

$$ln \, f_R = ln(\beta) - (E_a/k_B T) \qquad 4.11$$

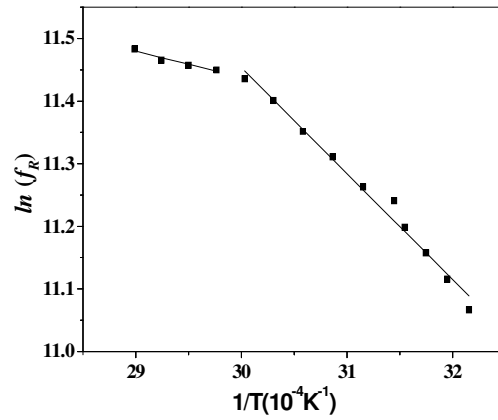where $\beta \simeq 1/2\pi A \sim w/8\pi^2 \eta_0 a^3$

Figure 4.24: The variation of $ln\ f_R$ versus 1/T for a mixture with 58 mol% of CP6B in a cell of thickness 6.8 μm. The filled squares correspond to the experimental points and two solid lines of different slopes have been fitted using equation 4.11.

We have plotted the values of ln f_R as a function of 1/T (where T is expressed in K) for a mixture with 58 mol% of CP6B in Figure 4.24. It can be noticed that there is a slope change in the plot at a temperature of about 60 ^{0}C. In this sample the N_lN_h transition using the scattered intensity was observed at ~ 65 ^{0}C (see Figure 4.10a). The two linear parts are fitted using equation 4.11 and are shown by solid lines. The activation energy $E_a \simeq 2.34 \times 10^{-13}$ ergs ($\simeq 0.15$ eV) and $\beta \simeq 15.1 \times 10^6$ Hz in the temperature range of 38 to 60 ^{0}C. Assuming the effective molecular radius $a \simeq 5$ Å, and $\eta_0 \simeq 1$ poise, the estimated nematic potential $w \simeq 1.49 \times 10^{-13}$ ergs ($\simeq 0.093$ eV) and activation energy due to viscosity, $w_{visc} \simeq 0.85 \times 10^{-13}$ ergs ($\simeq 0.053$ eV) . This value of E_a is much <u>lower</u> compared to that of a typical mesogen such as pentyl cyanobiphenyl (5CB) [6] which has $E_a \simeq 9 \times 10^{-13}$ ergs ($\simeq 0.56$ eV). In the temperature range of 63 to 72 ^{0}C, the values are reduced further to $E_a \simeq 0.58 \times 10^{-13}$ ergs ($\simeq 0.036$ eV), $\beta \simeq 0.33 \times 10^6$ Hz and $w \simeq 3.2 \times 10^{-15}$ ergs ($\simeq 0.002$eV) and $w_{visc} \simeq 0.54 \times 10^{-13}$ ergs ($\simeq 0.034$eV). It can be noted that the value of E_a measured in this temperature range is lower by about four times, and the value of nematic potential w is lower by two orders of magnitude compared to the

values at the lower temperatures. The nature of different types of short range order is reflected in different values of E_a. The nematic potential felt by 4PCPP in the higher temperature range is much smaller than that at low temperatures. These results indicate that there is a change of short range ordering in the medium around a temperature $\sim 60\ ^0$C. The values of activation energies and the nematic potentials are however too low and extremely unusual, and as such the Meier-Saupe model may not be appropriate. Hence we describe a different model used by Benguigui [10] and Diogo and Martins [11] to give an alternative interpretation.

According to the model of Benguigui [10], the relaxation phenomenon is related to the free volume. This theory relates the characteristic frequency ν_0 of reorientation of a particle and the twist viscosity γ_l. The reorientation consists in rotational jumps of π radians performed by the particle between two minima of the intermolecular mean field potential. The relation between γ_l and ν_0 is [11]

$$\gamma_1 = \frac{k_B T}{\pi^2 V_a} \frac{1}{\nu_0}$$

4.12

where k_B is the Boltzmann constant, V_a is the volume each particle must dispose in order to jump. The characteristic time $1/\nu_0$ is essentially the low-frequency dielectric relaxation time measured with electric field $\vec{E}$ parallel to the director $\hat{n}$. The above authors have taken into account both the nematic potential as well as the free volume factor and computed the rotational viscosity. As the temperature decreases, the available free volume per particle decreases due to a better packing of the molecules. They argue that when the temperature reaches some value T_0, γ_l becomes infinitely large and the nematic director would 'freeze' to a glassy state at this temperature if a phase transition did not occur at a higher temperature.

The relaxation frequency v_0 depends on the probability that the particle finds enough free volume to overcome the potential barrier [11] and is given by

$$v_0 \sim exp\left(-\gamma\frac{V_a-V_0}{V_N-V_0}\right) \sim e^{-\gamma} \, exp\left(-\gamma\frac{V_a-V_N}{V_N-V_0}\right) \qquad 4.13$$

where V_N is the volume per particle in the nematic phase, V_a-V_0 is the amount of free volume each particle must dispose in order to get to the activated state, V_N-V_0 is the free volume per particle, and γ is a factor lying between 0.5 and 1 to account for the free volume overlap. If α is the difference between the thermal expansion coefficients of the nematic phase and of the crystalline phase, then one can write

$$V_N(T)-V_0 \approx \alpha \cdot V_0(T-T_0) \qquad 4.14$$

where $V_0=V_N(T_0)$ and T_0 is the temperature at which there is no more free volume disposable.

If T_0 is not extremely low, the free volume factor dominates the temperature dependence of γ_1, and is given by [11]

$$\gamma_1 = g_1 \, S^2 exp\,[\theta S^2 / (T-T_0)] \qquad 4.15$$

where $\theta = \dfrac{V_a\gamma}{V_0\alpha}\dfrac{\beta u}{mV_N^3}$ is a constant which depends on the microscopic properties of the medium. γ is a factor which accounts for the free volume of overlapping allowed for each particle, β is the compressibility, u represents the strength of nematic potential [11].

Using equations 4.14 and 4.15 we can write the relaxation frequency as

$$ln \, f_R = ln \, B - [\theta S^2 / (T-T_0)] \qquad 4.16$$
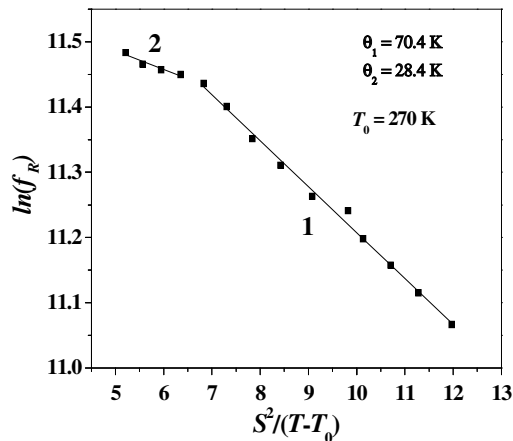
where B is a constant.

Figure 4.25: The variation of $ln\ f_R$ versus $S^2/(T\text{-}T_0)$ for a mixture with 58 mol% of CP6B in a cell of thickness 6.8 μm. The filled squares correspond to the experimental points and two solid lines of different slopes have been fitted using equation 4.16.

Using the estimated temperature variation of orientational order parameter S (see section 4.32) we have fitted the variation of $ln\ f_R$ versus $S^2/(T\text{-}T_0)$ data of the lower temperature region (denoted as 1 in Figure 4.25) to equation 4.14 and found that T_0=270K gives the best linear fit. The value of $T_{NI}\text{-}T_0$ =133K is similar to the values used by Benguigui (about 140K) [10]. We have fitted both low temperature as well as high temperature regions denoted as 1 and 2 (Figure 4.25) using the same value of T_0. The value of θ obtained for *low* temperature region is 70.4 K and that at *high* temperatures is 28.4 K. The value of B is ≈14.9 kHz at low temperatures and 11.2 kHz at high temperatures. The value of θ obtained for higher temperature region is lower by a factor of two compared to that at lower temperatures. As the observed relaxation frequency corresponds to that of 4PCPP, this difference in value of θ indicates that the free volume V_a needed to be disposed for reorientation is smaller i.e., the effective 'length' of the entity reorienting may be smaller at high temperatures than that needed at lower temperatures. The free volume available per particle, V_N at the higher temperature, of course is much higher than at lower temperatures, thus enhancing θ. The difference in θ again reflects a change in the short range order between the two regions.

4.313 Polarization measurement

We have carried out the polarization measurements using a triangular wave method to study if there is any polar short range order in the medium which can give rise to a measurable polarization. A triangular wave signal derived from a waveform generator (WAVETEK Model 39) was amplified using an amplifier (TREK model 601B-3). A resistance of 10 KΩ was connected in series with the cell and the current across the cell was measured using an oscilloscope (Tektronix TDS 220). The measurements were carried out on a mixture with 60 mol% of CP6B in a 3.4 μm cell, and a signal of V_{rms} = 40 V at 20 Hz frequency was used. The polarization (i.e., the dipole moment per unit volume) is the area under the peak in the current versus time plot divided by the electrode area of the liquid crystal cell .
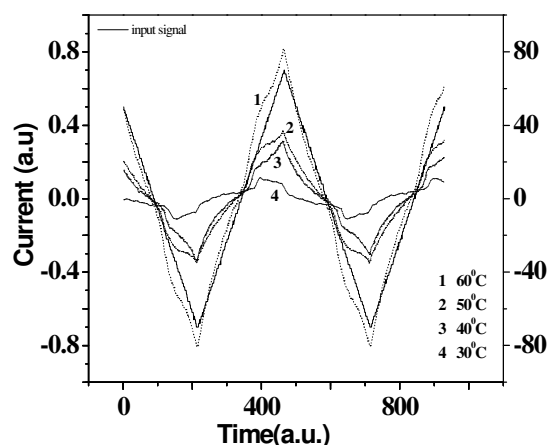

Figure 4.26: The plot of current as a function of time at various temperatures for a mixture with 60 mol% of CP6B in a 3.4 μm cell.

The plot of current versus time at various temperatures are presented in Figure 4.26. The triangular waveform drawn using the solid line represents the input signal. The curves drawn using dotted lines (numbered) correspond to the current measured at different temperatures. We can see broad peaks which may reflect polarization. However, the area under these peaks *decreases* with decreasing temperature. This shows that the peak arises due to ionic transport in the medium, whose contribution was already found in the dielectric studies (see Figure 4.23). Hence the polarization due to the short range order (if any) in the nematic medium is masked due to the dominant ionic polarization effect.

4.32   Planar aligned samples

We have carried out the optical path difference measurements on planar aligned samples of a few binary mixtures of CP6B with 4PCPP using the method described in section 4.22. The data from one such measurement on a 4.5μm thick sample of a binary mixture with 58 mol% of CP6B is shown in Figure 4.28. On cooling the sample from isotropic phase we have observed that a thin birefringent layer forms on the glass plate first, then small nematic domains start to grow and the whole sample becomes uniform as the sample is cooled further by about 2 - 3 ^{0}C. As the glass plates are coated with polyimide which is aromatic in nature, probably 4PCPP, the molecule with the *longer* aromatic core (see Figure 4.1) has a larger affinity towards the surface. A surface phase transition followed by bulk phase transition takes place in all the cells irrespective of the thickness of the cell. This is reflected as a slight slope change (Figure 4.27) and as a kink (Figure 4.28) at ~2 ^{0}C below the temperature at which the birefringence starts to increase.   The $N_l N_h$ transition occurs at 78.6 ^{0}C (Figure 4.27), which is seen as a jump in intensity.

Figure 4.27: Temperature variation of the ratio of transmitted intensity to reference intensity in a cell of thickness 4.5 μm of a binary mixture with 58 mol% of CP6B. The $N_l N_h$ transition at 78.6 ^{0}C is indicated by an arrow.

The intensity data from another measurement on a 5.4 μm thick sample with 62 mol% of CP6B is shown in Figure 4.28 in which the $N_l N_h$ transition occurs at 71.7 ^{0}C. The $N_l N_h$ transition temperature decreases with increasing concentration of CP6B in cells of similar thicknesses (Figures 4.27 and 4.28).
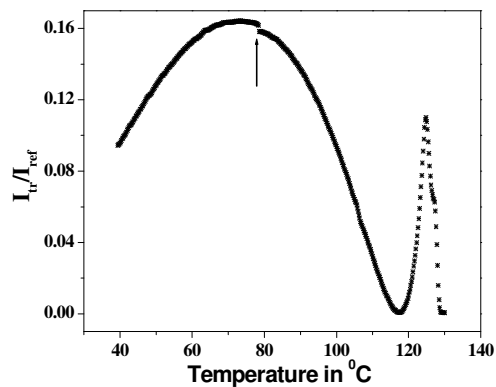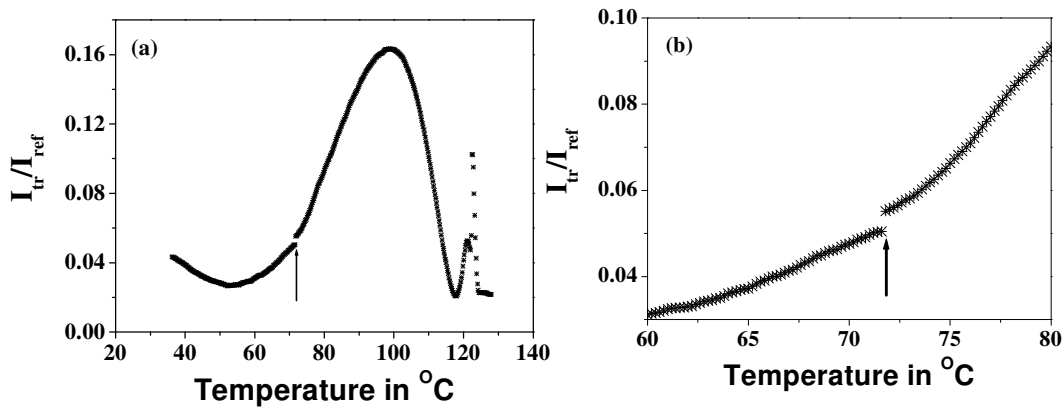
Figure 4.28: Temperature variations of the ratio of transmitted intensity to reference intensity in a cell of thickness 5.4 μm of a binary mixture with 62 mol% of CP6B (a) over the entire nematic range, (b) on an expanded scale around the N_lN_h transition.
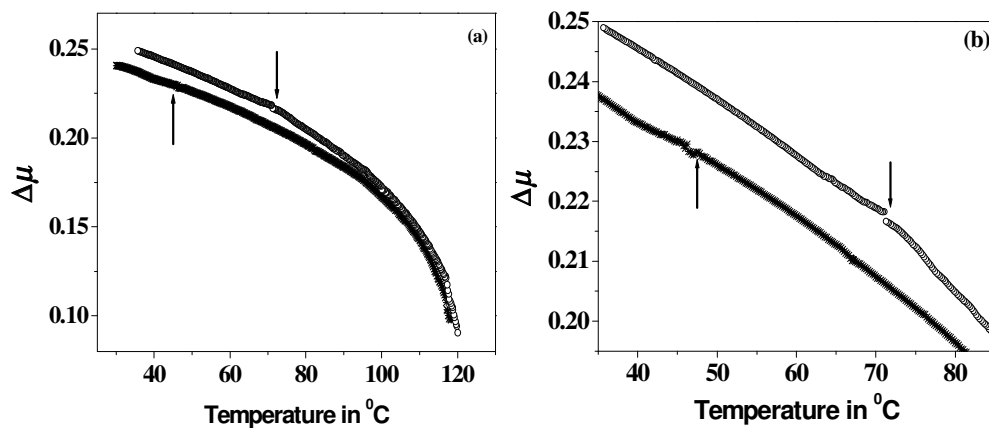
Figure 4.29: Temperature variations of birefringence $\Delta\mu$ of mixture with 62 mol% of CP6B in cells of thicknesses 5.4 μm (o) and 19 μm (✳) (a) in the entire nematic range (b) expanded around the N_lN_h transition (the N_lN_h transition is indicated by an arrow).

The temperature variations of birefringence $\Delta\mu$ estimated using the intensity data on cells of thicknesses 5.4 μm and 19 μm are shown in Figure 4.29. It may be noted that the $\Delta\mu$ in the 5.4 μm thick cell is larger compared to that measured in the 19 μm thick cell at low temperatures by up to ~ 5%. The N_lN_h transition occurs at ~ 46 ^{0}C in a cell of 19 μm thickness for a mixture with 62 mol% of CP6B (Figure

4.29). Thus it is obvious that the N_lN_h transition temperature depends strongly on the thickness of the sample in this geometry.

We have carried out *detailed* optical phase difference measurements on the binary mixture with 65 mol% of CP6B in cells of various thicknesses *t* ranging from 1.9 μm to 27 μm to investigate the effect of thickness of the sample on the N_lN_h transition. The transmitted intensity data on cells of eight different thicknesses are presented in Figures 4.30 - 4.33. The N_lN_h transition is seen as a jump in the intensity profile in cells with thickness $t \leq 8.4$μm. The N_lN_h transition is indicated by an arrow in each case.

Figure 4.30: Temperature variations of the ratio of transmitted intensity to reference intensity in cells of thicknesses 1.9 μm and 4.2 μm for a binary mixture with 65 mol% of CP6B. The N_lN_h transition occur at 88.4 ^{0}C and 66.8 ^{0}C in 1.9μm and 4.2μm thick cells (indicated by arrows) respectively.

As described earlier in section 3.2 (Chapter 3) the transmitted intensity of planar aligned sample placed between crossed polarisers at an azimuthal angle of 45^0 is given by $I=I_0(1-cos\Delta\phi)/2$, where $\Delta\phi=2\pi\Delta\mu t/\lambda$ is the optical phase difference. The transmitted intensity profile of a given compound shows a number of maxima and minima depending on the thickness *t* of the sample. The number of maxima and minima in the intensity profile increases with increasing thickness *t* of the sample. The first order N_lN_h transition appears as a jump in the intensity. Depending on the branch of the oscillation it occurs as a sudden increase (if in the increasing branch) or decrease (if in the decreasing branch) in the intensity. In Figure 4.30 the intensity

profile of the 1.9μm cell shows only one maximum and there is a jump in the intensity at 88.4 ^{0}C corresponding to N_lN_h transition indicating an increase in the order parameter in the lower temperature nematic. Such jumps can be noticed in cells of thicknesses 4.2μm (Figure 4.30), 6.1 μm and 8.4 μm (Figure 4.31) and the transition temperature decreases with increasing cell thickness.
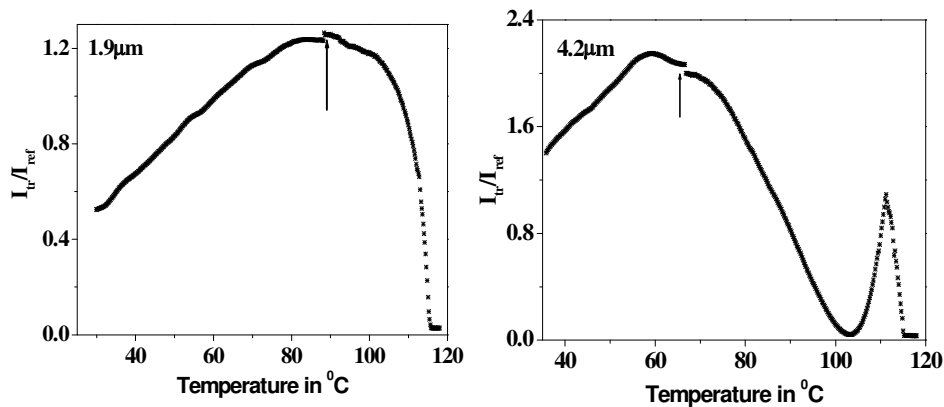

Figure 4.31: Temperature variations of the ratio of transmitted intensity to reference intensity in cells of thicknesses 6.1 μm and 8.3 μm for a binary mixture with 65 mol% of CP6B. The N_lN_h transition occur at 58.4 ^{0}C and 53.6 ^{0}C in 6.1 μm and 8.4 μm thick cells (indicated by arrows) respectively.

Figure 4.32: Temperature variations of the ratio of transmitted intensity to reference intensity in cells of thicknesses 13.3 μm and 15.6 μm for a binary mixture with 65 mol% CP6B.

For thicker cells with $t > 13\mu$m, as the transmitted intensity profile shows many maxima and minima, we present the intensity data in a small temperature range around the N_lN_h transition. The data presented on a 13.3 µm thick cell is shown in Figure 4.32, where the N_lN_h transition at ~ 45.5 ^{0}C is indicated by an arrow. It can be noticed that transmitted intensity below 50 ^{0}C *decreases* and shows a <u>minimum</u>. This dip in intensity can be seen more prominently in a cell of 15.6 µm thickness (Figure 4.32). Recalling our results on homeotropic samples (see Figures 4.6 - 4.12), this dip indicates a strong scattering of light from the sample around that temperature which in turn reduces the *transmitted* intensity. The photodiode (Centronics model OSD-5) used to monitor the transmitted intensity has a relatively small cathode area ~10 mm^2 and hence probably the measured <u>transmitted</u> intensity will not be affected by the *scattered* intensity. We have indicated the probable temperature variation of the transmitted intensity *in the absence* of scattering of light around that temperature by a *dash-dotted* line. We consider the temperature at which there is a minimum in the transmitted intensity to be the N_lN_h transition temperature (Figures 4.32 – 4.33). The absence of a jump in the transmitted intensity indicates that the N_lN_h transition is *no longer* a first order transition. As the thickness of the sample is further increased it can be noticed that the dip in the intensity decreases (Figure 4.33).
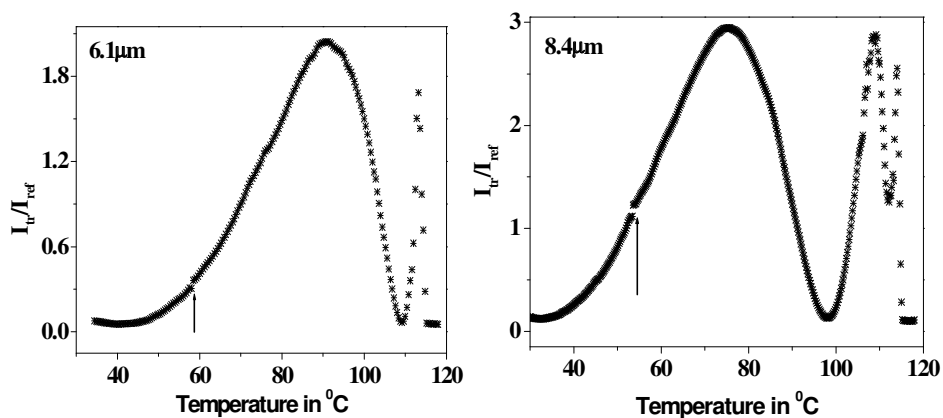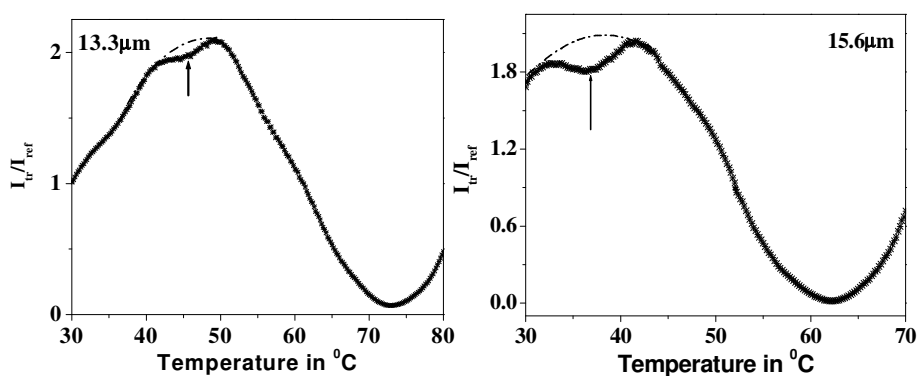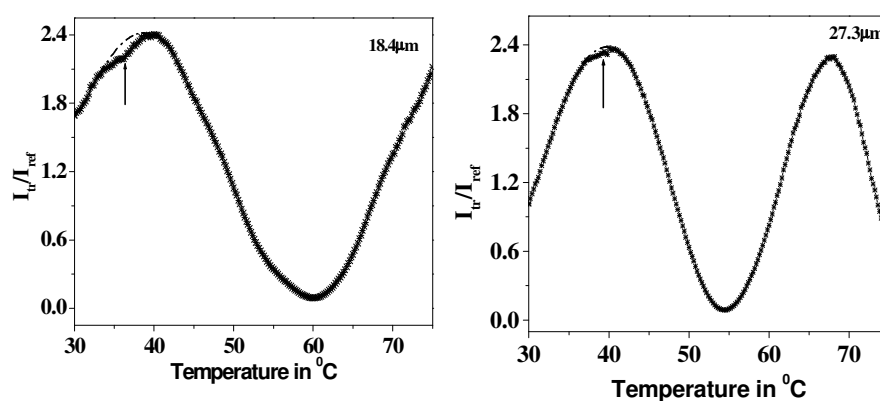
Figure 4.33: Temperature variations of the ratio of transmitted intensity to reference intensity in cells of thicknesses 18.4 µm and 27.3 µm for a binary mixture with 65 mol% of CP6B.
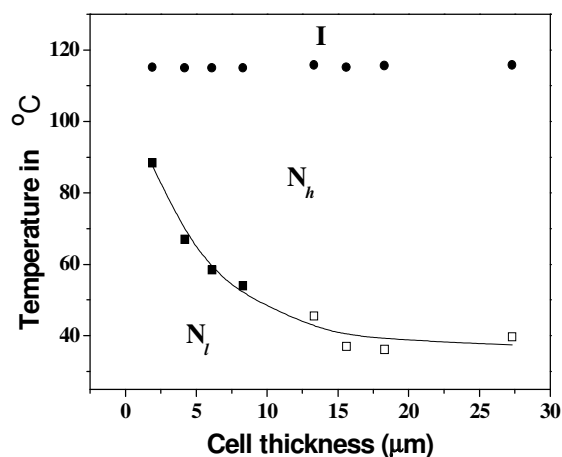
Figure 4.34: The variations of N_hI and N_lN_h transition temperatures as functions of sample thickness for the mixture with 65 mol% of CP6B. The symbol ■ corresponds to experimental data on cells with $t \leq 8.4\mu m$ (exhibiting a jump in the transmitted intensity) and □ corresponds to $t > 13\mu m$ (exhibiting a dip in the transmitted intensity). The solid line corresponds to a least squares fit to an exponential function (see text).

The variations of the N_lN_h and N_hI (usually indicated as NI) transition temperatures as functions of sample thickness t for the binary mixture with 65 mol% of CP6B are shown in Figure 4.34. It may be noted that the NI transition temperature is practically a constant as a function of cell thickness. The N_lN_h transition temperature increases with decreasing thickness of the sample varying slowly at first from $t = 27.3\mu m$ to $t \approx 10\mu m$. For cells with thickness t below 10μm the N_lN_h transition temperature is *enhanced* <u>increasingly rapidly</u>. We have fitted the variation of the N_lN_h transition temperature with sample thickness t to an exponential function of the form $T=T_0+T_1e^{-(t/h)}$ where T_0, T_1 and h are the fit parameters. The values of the fit parameters are $T_0 = 37.1\ ^0C$, $T_1 = 73.6\ ^0C$ and $h= 5\ \mu m$.
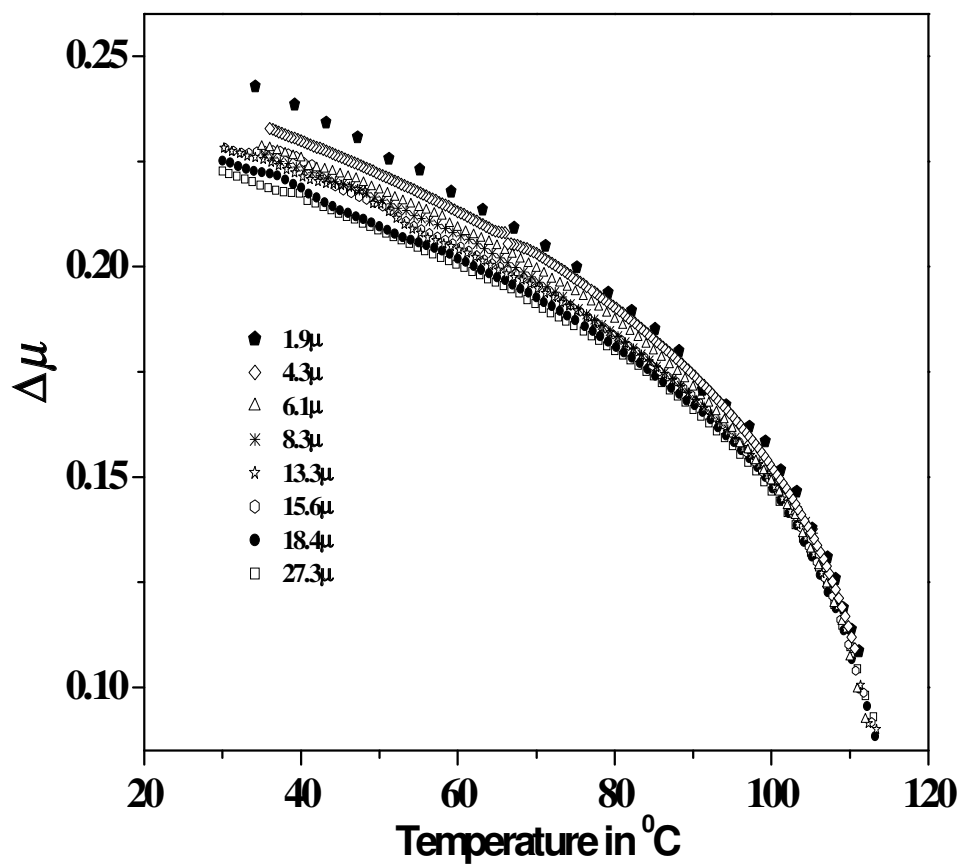
Figure 4.35: Temperature variations of birefringence $\Delta\mu$ of the binary mixture with 65 mol% of CP6B for cells of various thicknesses from 1.9 μm to 27.3 μm
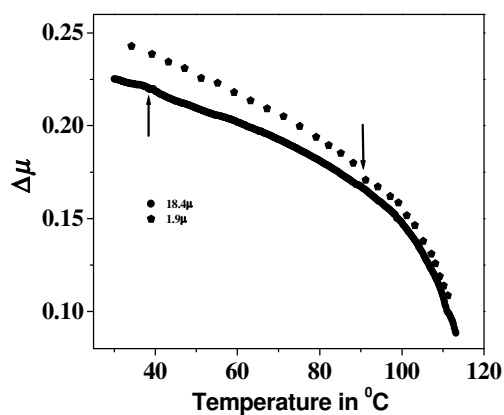
Figure 4.36: Temperature variations of birefringence $\Delta\mu$ of the binary mixture with 65 mol% of CP6B for cells of thicknesses 18.4 μm and 1.9 μm.

The birefringence $\Delta\mu$ as a function of temperature of the binary mixture with 65 mol% of CP6B for various thicknesses are shown in Figure 4.35. It can be noticed that the value of $\Delta\mu$ at any given temperature increases with decreasing cell thickness. The enhancement <u>increases</u> as the temperature is lowered. The value of $\Delta\mu$ measured in a 1.9 μm thick cell is enhanced by upto ~ 9% compared to that measured in a cell of thickness t = 18.4 μm at a temperature of ~ T_{NI}-80 ^{0}C. For clarity, in Figure 4.36 we present the data of only two cells of thicknesses 18.4 μm and 1.9 μm.
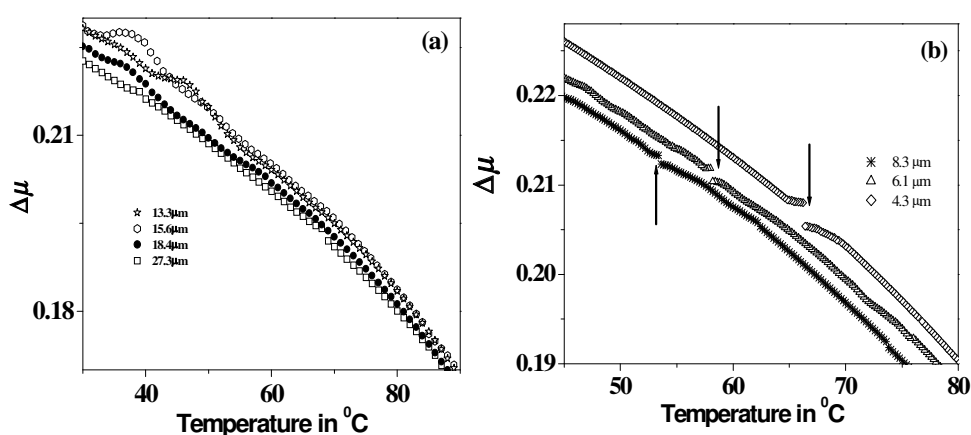
Figure 4.37: Temperature variations of the 'birefringence' $\Delta\mu$ of binary mixture with 65 mol% of CP6B on an expanded scale around N_lN_h transition (a) in cells of thickness lying between 13.3 μm to 27.3 μm. (b) for cells of thicknesses 4.3 μm, 6.1 μm and 8.3 μm. The N_lN_h transition is indicated by arrows.

In Figure 4.37 we show the birefringence data on an expanded scale in the temperature range around the N_lN_h transition temperature. The data on cells of thickness $t > 13$μm in which the N_lN_h transition is *no longer* a first order transition are shown in Figure 4.37a. As the transmitted intensity data around the N_lN_h transition is reduced due to the *scattering* of light from the sample, the calculation of $\Delta\mu$ using the transmitted intensity data in that temperature range is *incorrect* and shown only to locate the N_lN_h transition temperature.

In Figure 4.37b we show the birefringence data on an expanded scale around the $N_l N_h$ transition for three cells with thicknesses 4.3 μm, 6.1 μm and 8.4 μm. It can be noticed from Figure 4.37b that the jump in the value of $\Delta\mu$ at $N_l N_h$ transition rapidly decreases with increasing thickness of the cell. This indicates that the strength of the first order transition decreases with increase of the thickness t, which acts as an external control parameter and at some critical thickness t_c, the transition ends in a *critical point*. Beyond t_c, the medium continuously evolves from one type of N to the other, but the strong scattering of light from the sample (Figures 4.32 - 4.33) indicates that there is a rapid variation of the short range order in the supercritical region around some temperature. We define the percentage jump in $\Delta\mu$ at $N_l N_h$ transition $[\delta(\Delta\mu)] = \dfrac{\left(\Delta\mu_{N_h} - \Delta\mu_{N_l}\right)}{\Delta\mu_{N_h}} \times 100$. We found that the cube root of $\delta(\Delta\mu)$ i.e., $\sqrt[3]{\delta(\Delta\mu)}$ at $N_l N_h$ varies approximately linearly with the cell thickness. Fitting the data to $\sqrt[3]{\delta(\Delta\mu)} = a(t_c - t)$, where a is a constant (Figure 4.38) we can estimate t_c. The value of critical thickness t_c is found to be ~ 15 μm. Indeed as seen in Figure 4.32 for a cell with thickness t =15.6 μm the dip in the intensity is very prominent indicating a strong scattering of light from the sample for that thickness. We have however not made a detailed study around this thickness to pinpoint t_c.
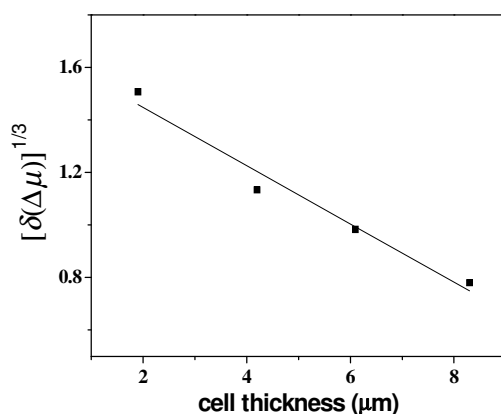
Figure 4.38: The variation of $\sqrt[3]{\delta(\Delta\mu)}$, the cube root of the percentage jump in $\Delta\mu$ at the $N_l N_h$ transition as a linear function of cell thickness.
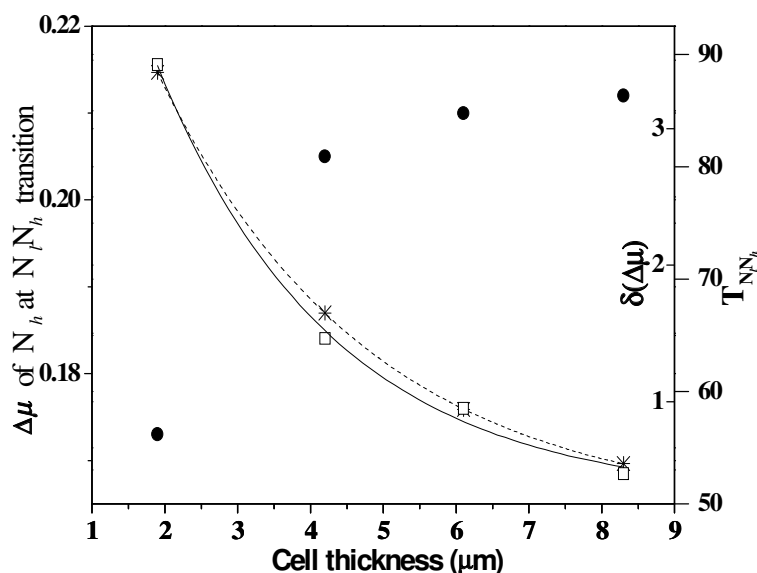
Figure 4.39: The variations of $\Delta\mu$ of the N_h phase at N_lN_h transition, the percentage jump in birefringence $\delta(\Delta\mu)$ at N_lN_h transition and the N_lN_h transition temperature as functions of cell thickness. The symbol • corresponds to $\Delta\mu$ of the N_h phase at N_lN_h transition, ✳ corresponds to N_lN_h transition temperature and □ corresponds to the percentage jump in birefringence $\delta(\Delta\mu)$ at N_lN_h transition.

The value of $\Delta\mu$ of the N_h phase at the first order N_lN_h transition temperature increases with sample thickness as shown in Figure 4.39. This trend is opposite to that of the percentage jump in $\Delta\mu$ i.e., $\delta(\Delta\mu)$. The opposite trend is a consequence of the lowering of the N_lN_h transition temperature with increase of thickness. The trends in T_{NN}, $\Delta\mu$ as well as $\delta(\Delta\mu)$ are shown in Figure 4.39 for comparison. We have not yet carried out similar studies on the other compositions of the binary mixtures.

In Figure 4.40 we present the intensity data from measurements on thick cells with $t{\sim}19$ μm for binary mixtures with three different concentrations of CP6B. The N_lN_h transition is a first order transition characterised by a jump in the transmitted intensity for the binary mixtures with concentrations of 54 mol% and 62 mol% of

CP6B. Thus, the critical thickness for these concentrations appears to be larger than 19 μm. As seen in Figure 4.40c, the N_lN_h transition for the mixture with 49 mol% of CP6B appears as a slope change rather than as a jump. One probable reason may be that in the area illuminated by the laser beam the thickness of the cell may not be uniform. The transition temperature is thickness sensitive and as such may get smeared out and appear as a slope change. As already discussed above for a mixture with 65 mol% of CP6B a dip in the intensity profile is seen (Figure 4.33) i.e., it is in the supercritical region.
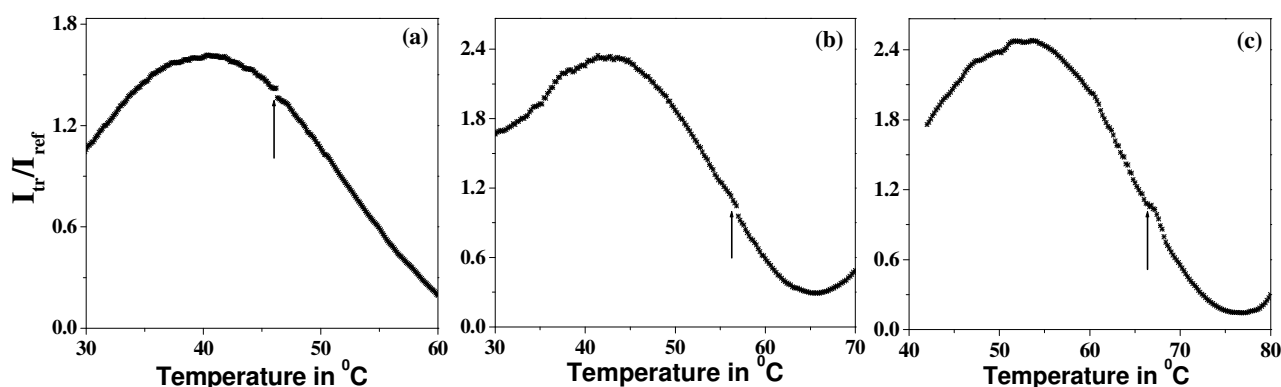
Figure 4.40: Temperature variations of the ratio of transmitted intensity to reference intensity in cells with thickness t ~19 μm for binary mixture with (a) 62 mol% of CP6B (b) 54 mol% of CP6B and (c) 49 mol% of CP6B.

The estimated values of birefringence $\Delta\mu$ using planar aligned samples of thickness ~ 19 μm as functions of temperature for the four concentrations of binary mixtures of CP6B and 4PCPP are shown in Figure 4.41a. The temperature variation of $\Delta\mu$ in a small temperature range around the N_lN_h transition are shown in Figure 4.41b. The birefringence values of mixtures for temperatures within ~$T_{NI} - 2\,^0C$ are not presented because of the coexistence of nematic and isotropic phases in that temperature range.
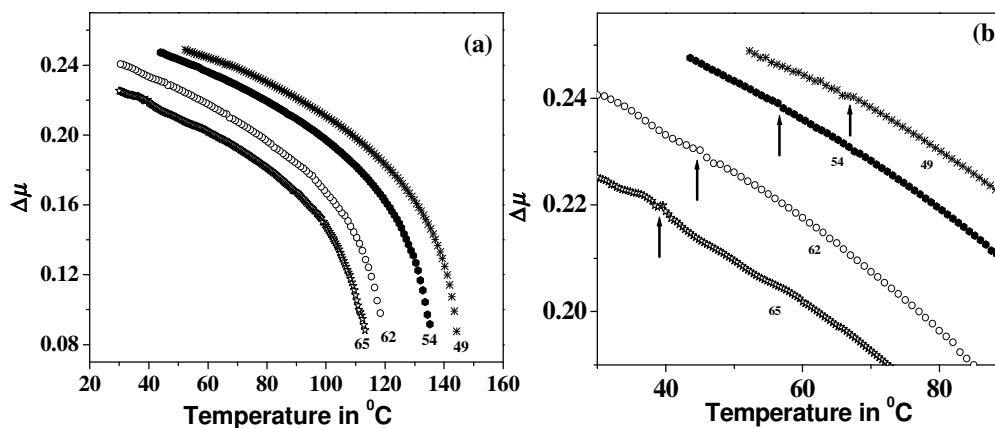
Figure 4.41: Temperature variations of birefringence $\Delta\mu$ for binary mixtures of CP6B with 4PCPP (a) over the entire nematic range and (b) on an expanded scale near N_lN_h transition temperatures, which are indicated by arrows. The numbers inside the plots indicate the concentration of CP6B in mol percentage. The thickness of the cell is ~19 μm in each case.
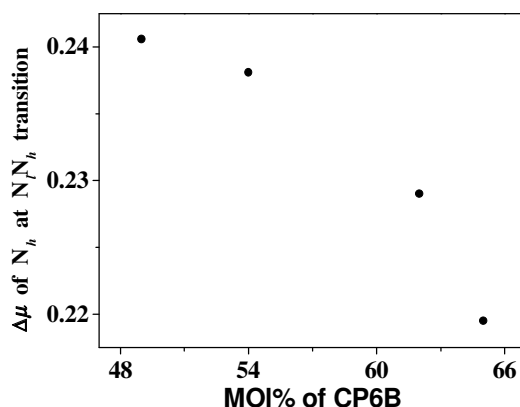
Figure 4.42: The variation of $\Delta\mu$ of the N_h phase at N_lN_h transition in planar aligned thick cells with t ~19 μm as function of concentration of CP6B.

In Figure 4.42 we present the data of $\Delta\mu$ of the N_h phase at the N_lN_h transition temperature in planar aligned thick cells, with t ~19 μm as a function of molar concentration of CP6B. The value of $\Delta\mu$ decreases with increase in concentration of CP6B, the compound with relatively lower optical anisotropy. The difference between the NI and N_lN_h transition temperature decreases only slightly from ~ 80 ^{0}C to ~ 77 ^{0}C with decreasing concentration of CP6B.

We have fitted the temperature variations of $\Delta\mu$ values of the four binary mixtures to Haller's extrapolation formula (see equation 2.6). The estimated values of T^t, the exponent β and $\Delta\mu_0$ are tabulated along with T_{NI} in Table 1. The value of T^t-T_{NI} increases from 1.1 ^{0}C to 1.4 ^{0}C with increase in concentration of CP6B, and the exponent β is ~ 0.24. The value of $\Delta\mu_0$ decreases from 0.36 to 0.33 with increase in concentration of CP6B.

Concentration of CP6B (mol%)	T_{NI}(K)	T^t(K)	β	$\Delta\mu_0$
49	417.2	418.3	0.24	0.36
54	408.2	409.5	0.24	0.36
62	392.4	393.7	0.24	0.34
65	386.2	387.6	0.24	0.33

Table 1: The table of estimated values of T^t, the exponent β and $\Delta\mu_0$ for the four binary mixtures estimated using Haller's extrapolation formula.
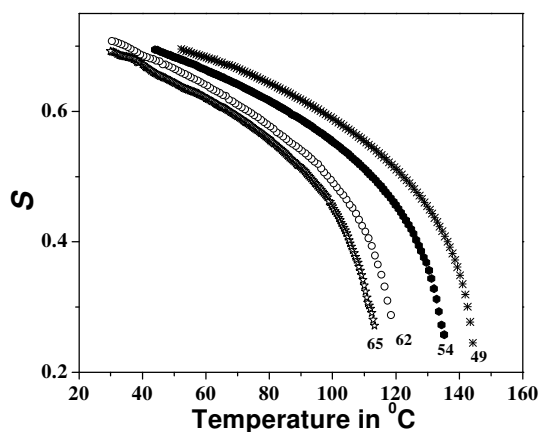
Figure 4.43: Temperature variations of orientational order parameter S for the four binary mixtures of CP6B with 4PCPP. The numbers inside the Figure indicate the concentration of CP6B in mol percentage.

The temperature variations of orientational order parameter S ($\approx\Delta\mu/\Delta\mu_0$) of the four binary mixtures are calculated using the $\Delta\mu_0$ values estimated as above (Table 1). The results are shown in Figure 4.43. The value of S at N_lN_h transition is ~ 0.67 for all the four mixtures.
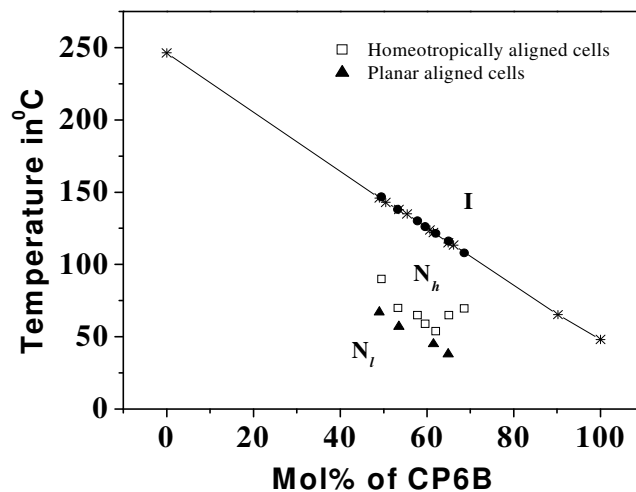
Figure 4.44: The concentration-temperature phase diagram of binary mixture of CP6B and 4PCPP. The transition temperature data from both homeotropically aligned as well as planar aligned cells are given for comparison.

We show the phase diagram of the binary mixtures in both homeotropic and homogeneously aligned cells of thickness with $t \sim 19\mu$m in the latter case, in Figure 4.44. The $N_l N_h$ transition temperatures in planar aligned thick samples with $t \sim 19\mu$m for all the compositions on which measurements have been carried out are lower than those observed for homeotropically aligned samples. T_{NI} increases by 2 ^{0}C with every 1 mol% decrease in concentration of CP6B. In planar aligned cells the $N_l N_h$ transition temperature also increases linearly by 1.6 ^{0}C for 1 mol% decrease in concentration of CP6B in a concentration range of 49 – 65 mol% of CP6B. The reduced temperature $T_r = T(K)/T_{NI}(K)$, at which the $N_l N_h$ transition in planar aligned cells occurs in all the four mixtures is $\sim$ 0.8. But for homeotropically aligned cells the variation shows a minimum at a composition $\sim$ 62 mol% of CP6B. The $N_h I$ transition temperature is independent of the sample geometry.

4.33   X-ray studies

The Nematic- Nematic transition is characterised by a change in short range ordering i.e., in the association of neighbouring molecules. We have carried out a preliminary x-ray study on a binary mixture to explore the short range order. The x-ray diffraction studies were conducted   with CuK_α radiation ($\lambda=1.54\text{Å}$) using a rotating anode generator (Rigaku Ultrax 18) and an image plate (Marresearch). The binary mixture with 60 mol% of CP6B was taken in a thin-walled glass capillary tube of   0.5 mm diameter (Hampton Research: model HR6-112). A magnetic field of ~ 2.3 kgauss was applied in a direction orthogonal to the incident x-ray beam to get an oriented sample. The sample was heated to the isotropic phase and cooled down in the presence of the magnetic field and measurements at a few temperatures starting from 100 ^{0}C to 38 ^{0}C were carried out. The x-ray diffraction pattern of the oriented sample at a temperature of ~50 ^{0}C is shown in Figure 4.45. As expected for a nematic sample, two pairs of diffused arcs in orthogonal directions can be seen. The outer arcs seen at the periphery are fainter than the inner arcs. (A diffuse arc seen at the bottom-right at an intermediate radius is an artifact due to a defect in the image plate.) The intermolecular spacing r obtained using the outer diffused arcs is found to be ~ 4.5 Å which is a typical width of a rod like molecule. The spacing d got using the inner arcs which corresponds to the layer spacing of short range ordered groups (see Figure 3.1, chapter 3) is ~26.3 Å. Surprisingly *no noticeable* change was seen in the value of d in the entire temperature range of the nematic phase. (Due to a breakdown in our X-ray experimental setup we have not been able to carry out measurements on mixtures with other compositions, which will be taken up later.)

Figure 4.45: The X-ray diffraction pattern of a binary mixture with 60 mol% of CP6B at 50 ^{0}C cooled in presence of 2.3 kgauss magnetic field.

Biswanath Jha et al [12] have carried out X-ray diffraction measurements on the pure compound 4PCPP. They report that layer spacing d of short range ordered groups <u>decreases</u> on decreasing the temperature. The length of the molecule in its fully extended form is l ~18.8 Å. The value of d changes slowly from ~22.4 to 24 Å as the temperature is increased from 90.5 to 185 ^{0}C. Beyond 185 ^{0}C, d increases sharply and reaches a value of ~ 32.3 Å (d~1.7l) at 240 ^{0}C. This clearly indicates that in pure 4PCPP there is a change in short range ordering from a shorter to a larger partial bilayer structure as the temperature increases, in agreement with the results on some other compounds with polar end groups (see Figure 3.1). As such, the constancy of d in the binary mixture obtained by us is quite surprising.

Using the ACD/Chemsketch software (freeware version 5.12) optimized molecular structures of both 4PCPP and CP6B are generated (Figure 4.46). The length of the entire molecule and that of the aromatic core of (a) 4PCPP are 18.8Å and 13.8Å respectively and   (b) for CP6B the values are 19.4Å   and 11.8Å respectively. Assuming an overlap of the aromatic moities, the spacing d for partial bilayer antiparallel structure formed from a pair of 4PCPP molecules d will be ~23.8Å, and that for a pair of CP6B molecules will be 27 Å, and that for a pair of 4PCPP with CP6B will be 26.4 Å . These d values are quite close to each other. The layer spacing obtained by us using X-ray measurements on binary mixture with 60 mol% of CP6B   is ~26.3 Å and implies that the medium consists of antiparallel structures of different types. The X-ray results do not indicate the 'monolayer' structure which could have occurred if the low temperature phase was the N_1 phase.
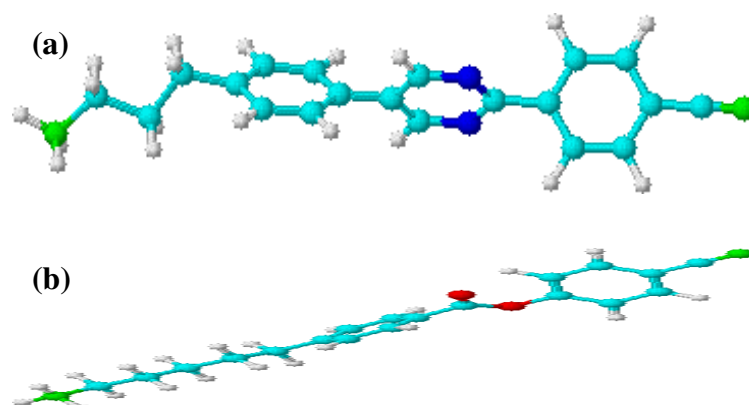
Figure 4.46: The molecular structures of (a) 4PCPP and (b) CP6B generated and optimized for 3-dimensional optimization using ACD/Chemsketch software.

As mentioned above the birefringence $\Delta\mu$ which is a measure of orientational order parameter S in thin cells is enhanced compared to that in thick cells (Figure 4.35). The increase in N-N transition temperature appears to be partly associated with the enhancement of order parameter in thin cells. Before discussing the implications of our experimental observations on the NN transition we would like to present a brief description about some theoretical models [13-14] and earlier experimental observations [15-17] on the enhancement of order parameter in thin cells.

4.4 Enhancement of order parameter of nematics confined in thin cells

A uniformly oriented nematic sample has no spatial variation of director $\hat{n}$. There are many theoretical and some experimental reports which show that the orientational order parameter S at a surface treated for alignment of nematic director is enhanced compared to that in the bulk [15-17]. Ping Sheng [13,14] has extended the Landau-de Gennes (LdG) theory of nematics by adding a surface potential term, which enhances the order parameter at the surface (see section 4.42). He found that within a limited range of surface potentials a surface transition can occur at a temperature higher than that of the bulk transition. Close to the nematic-isotropic (NI) transition point, the surface-induced order decays to the bulk value over a length scale, which is an order of magnitude larger than the order parameter correlation length ξ_0 [13,14]. In the nematic phase S at the surface of the substrate as well as in the interior of the sample increases with decreasing sample thickness.

Mada and Kobayashi [15] measured the temperature variations of refractive indices μ_e and μ_o using an interferometric technique in nematic as well as in the isotropic phase of heptyl cyanobiphenyl (7CB) taken in *planar* aligned cells. The estimated value of S at surface is found to be ~0.15 just above T_{NI} and had finite values even at temperatures far above T_{NI}. In the nematic phase the value of S at the surface is found to be always 25% higher than that measured in the bulk [15].

Sobha et al [16] reported that birefringence $\Delta\mu$ of CP7B measured in a *planar* aligned 1.5 μm thick cell is enhanced by ~15% compared to that of an 18 μm thick cell in the entire nematic range. Recently Dhara et al [17] have carried out $\Delta\mu$

measurements on mesogens with different chemical structures having either longitudinal or transverse dipole moments. They found that the $\Delta\mu$ measured in *planar* aligned thin cells of $t \sim 1.5$ μm is larger by $\sim 10\%$ with respect to that in thick cells ($t \geq 7$ μm) at temperatures $T_{NI} - 12$ ^{0}C (and even lower) for mesogens with <u>aromatic</u> cores irrespective of the orientation of dipole moment in the molecule.

The enhancement of $\Delta\mu$, which is a measure of the orientational order parameter S, in thin cells compared to that in thick cells can arise for two reasons [17]: (i) suppression of the thermal fluctuations of the director $\hat{n}$ in thin cells (ii) as mentioned above the enhanced surface order increases the measured $\Delta\mu$ in thin cells.

4.41 Quenching of director fluctuations in thin cells

As mentioned in section 4.1, in the nematic phase there are thermal fluctuations of the director $\hat{n}$. These fluctuations cause strong light scattering (10^6 times larger than the scattering by an isotropic fluid) [1]. As a result the nematic is turbid in appearance.
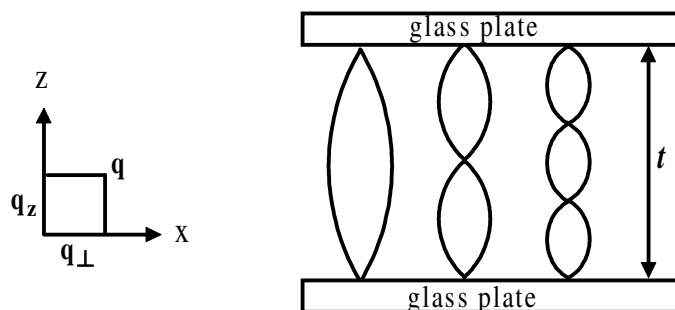
Figure 4.47: Schematic representation of a few allowed modes of fluctuation between two plane surfaces.

In the one constant approximation [1] we can write the distortion energy density as

$$F_d = \frac{1}{2} K \left(\nabla n_\perp \right)^2 \qquad\qquad 4.17$$

where $n_\perp$, is the fluctuation in a direction perpendicular to the director (assumed to be along the z- axis) . It is convenient to analyse $n_\perp$ in Fourier components

$$n_\perp(\vec{q}) = \frac{1}{V} \int n_\perp(\vec{r}) \, e^{i\vec{q}.\vec{r}} \, d\vec{r} \, . \tag{4.18}$$

From equations 4.17 and 4.18, we get

$$F(q) = \frac{1}{2} K \, q^2 n_\perp^2(q) V \tag{4.19}$$

where V is the volume. Using equipartition theorem i.e. equating the energy of each mode with the thermal energy $\frac{1}{2} k_B T$, we get

$$\left\langle \left| n_\perp(q) \right|^2 \right\rangle = \frac{k_B T}{V K q^2} \tag{4.20}$$

where k_B is the Boltzmann constant, T the temperature, V the volume, and K is the elastic constant. The wave vector $\vec{q}$, can be decomposed into q_z, along the z axis and $q_\perp$, which is in the xy plane (Figure 47). A schematic representation of a few fluctuation modes with allowed values of q_z are shown in Figure 4.47. Any mode which has a wavelength $(2\pi / q_z)$ larger than twice the cell thickness t is not allowed, due to the confinement along the z direction. Hence the number of modes are reduced when the sample thickness t is decreased.

In principle, to calculate the r.m.s. fluctuation in real space, we have to sum over the allowed modes along the z direction (Figure 4.47) [18]. However, as the smallest gap t used in the experiment is >1 μm which is much larger than the intermolecular distance a ($\approx 20 \times 10^{-8}$ cm), the summation is replaced by an integration over the appropriate limits. In real space the fluctuation amplitude [17] is given by

$$\left\langle \left| n_\perp(r) \right|^2 \right\rangle = \frac{k_B T}{8\pi^3 K} \int\limits_{\pi/t}^{q_{max}} dq_z \int\limits_0^{q_{max}} \frac{2\pi q_\perp dq_\perp}{q_\perp^2 + q_z^2} \tag{4.21}$$

where $q_{max} \approx 2\pi / a$, is the cut off wave vector. Integrating over $q_\perp$ we get,

$$\left\langle \left| n_\perp(r) \right|^2 \right\rangle = \frac{k_B T}{8\pi^2 K} \int\limits_{\pi/t}^{q_{max}} \left[ln\left(1 + \frac{q_{max}^2}{q_z^2} \right) \right] dq_z \tag{4.22}$$

As $t \approx 1 \mu m$, $q_{max} t \approx 10^3$. We use this to simplify the above integral to get

$$\left\langle \left| n_\perp(r) \right|^2 \right\rangle \approx \frac{k_B T}{8\pi^2 K} \left[q_{max} \left(\ln 2 + \frac{\pi}{2} \right) + \frac{2\pi}{t} \left\{ \ln\left(\frac{\pi}{t q_{max}} \right) - 1 \right\} \right] \qquad 4.23$$

From equation 4.23 it is clear that the fluctuation amplitude is reduced with the reduction of the sample thickness t. Using equation $\left\langle n_z^2 \right\rangle = 1 - 2\left\langle n_\perp^2 \right\rangle$, the measured value of the order parameter can be written as $S_{meas} = S_0 \left(3\left\langle n_z^2 \right\rangle - 1 \right)/2$ where S_0 is the order parameter in the absence of director fluctuations as calculated for example, in a mean field theory. We get the order parameter in a finite thickness cell t as $S_{meas} = S_0 \left(1 - 3\left\langle \left| n_\perp(r) \right|^2 \right\rangle \right)$. Using equation 4.23 the order parameter S_{meas} can be written as

$$S_{meas} = S_0 \left[1 - \frac{3k_B T}{8\pi^2 K} \left(q_{max} \left(\ln 2 + \frac{\pi}{2} \right) + \frac{2\pi}{t} \left\{ \ln\left(\frac{\pi}{t q_{max}} \right) - 1 \right\} \right) \right] \qquad 4.24$$

Using $K=5\times10^{-7}$ dynes, $a = 20$ Å, and $T=330$ K, the order parameter is found to increase by ~0.1% in 1μm cell compared to that in 10 μm cell. But experimentally we find that the order parameter in a thin cell of $t =1.9$ μm is *enhanced* by ~9% compared to that in thick cell of $t \sim 19$ μm (see Figure 4.35). As such the enhancement of order parameter due to the partial quenching of the director fluctuations in thin cells can not explain the experimental result.

Now we consider the effect of confinement on the order parameter of nematic liquid crystals due to the alignment at the walls. We mentioned above that using the Landau de Gennes theory Ping Sheng calculated the order parameter profile in thin cells [13,14]. He restricted the calculation between T_{NI} -0.12^0 to T_{NI} +0.36^0. Dhara et al [17] have extended the calculation to a few degrees below T_{NI} to see the effect of confinement on the order parameter. We present a brief discussion about this model as adapted from Dhara et al [17]. We also add another additional term arising due to order electricity in the free energy density which however does not make much difference to the predicted results.

4.42 Landau de Gennes Theory of a nematic liquid crystal confined between two plane parallel plates with a large surface orientation potential

We consider a nematic liquid crystal confined between two plane parallel surfaces separated by a distance t. The solid-liquid crystal interfaces are defined by $z = 0$ and $z = t$ (Figure 4.47). The sample is assumed to be uniform in x and y directions. The substrates are treated such that the molecules experience a uniaxial aligning potential in a particular direction say, for example along x-axis (Figure 4.47). The surface potential experienced by each molecule can be expressed in general as [13]

$$V = \langle v(\theta, z) \rangle = -G\delta(z)\langle P_2(\cos\theta) \rangle = -G\delta(z)S \qquad 4.25$$

where the angular brackets represent a local average, G represents the strength of surface potential and $\delta(z)$ implies that surface potential is assumed to be short range in nature. As experimentally found the enhancement of order parameter in thin cells is very substantial (Figure 4.35), we assume the surface potential is so large that there is perfect order at the surface i.e. $S(t) = S(0) = 1$. Selinger et al [19] calculated the variation of order parameter from the surface to the bulk assuming a strong surface potential ($V_S = 10V_0$, where V_0 is the Maier-Saupe orientation potential between the molecules). It was found that at the surface the order parameter is saturated i.e. $S(0) = 1$. However, they did not extend the molecular theory to the nematic phase. Following the method described by Sheng [14], the Landau-de Gennes free energy density can be written as

$$\varphi = f(S) + L\left[\frac{dS}{dz}\right]^2 \qquad 4.26$$

where $$f(S) = \frac{\alpha}{2}(T - T^*)S^2 - \frac{B}{3}S^3 + \frac{C}{4}S^4 \qquad 4.27$$

$f(S)$ is the bulk free energy density and α, T^* B, C are material parameters (see Chapter 1). L is the bare elastic constant. The total free energy per unit area (Φ/A), for a given φ is got by integrating over z:

$$\frac{\Phi}{A} = \int_0^t \left[f(S) + L\left[\frac{dS}{dz}\right]^2 \right] dz \qquad 4.28$$

The Euler–Lagrange equation for the minimization of (Φ/A) is given by

$$\frac{\partial\varphi}{\partial S} = \frac{\partial}{\partial z}\left(\frac{\partial\varphi}{\partial\left(\frac{\partial S}{\partial z}\right)} \right) \qquad 4.29$$

Using equations 4.26 and 4.27 we get,

$$\frac{\partial f(S)}{\partial z} = 2L\left(\frac{d^2 S}{dz^2}\right)\left(\frac{dS}{dz}\right) \qquad 4.30$$

Equation 4.30 can be integrated once to get

$$L\left(\frac{dS}{dz}\right)^2 = f(S) + \Omega \qquad 4.31$$

where Ω is an integration constant and is determined by the following boundary conditions [14]

$$S=1 \qquad \text{at} \qquad z=0, t$$

$$\left[\frac{dS}{dz}\right]_{z=t/2} = 0 \quad \text{and} \quad S(t/2) = S_m, \qquad 4.32$$

S_m is the minimum order parameter which is obtained at the mid-plane of the sample. Using the above boundary conditions in equation 4.31 we get,

$$L\left(\frac{dS}{dz}\right)^2 = f(S) - f(S_m) \qquad 4.33$$

Dividing both sides by αT_{NI}, we get a dimensionless equation, which is given by

$$\xi_0^2\left(\frac{dS}{dz}\right)^2 = F(S) - F(S_m) \qquad 4.34$$

where $\xi_0 = \sqrt{\dfrac{L}{\alpha T_{NI}}}$, is the bare correlation length and $F(S) = \dfrac{f(S)}{\alpha T_{NI}}$ and

$F(S_m) = \dfrac{f(S_m)}{\alpha T_{NI}}$.

On integrating equation 4.34, $S(z)$ profile is obtained

$$\frac{z}{\xi_0} = \int_{S(z)}^{1} \sqrt{\frac{1}{F(S) - F(S_m)}} \; dS \qquad 4.35$$

The material parameters α, B, C for 4-pentyl-4' -cyanophenylcyclohexane (PCH5) are assumed to be $\alpha = 0.1$ J/cm^3-K, $B = 1.5$ J/cm^3, $C = 3.8$ J/cm^3, $T^* = 327.2$K, $T_{NI} = 328.5$ K. The first three coefficients are of the same order as in other nematics [13]. The bare elastic constant L, is found by using the formula [20]

$$L = \frac{1}{2}\left[\frac{K_{11} + K_{22} + K_{33}}{3S^2}\right] \qquad 4.36$$

where K_{11}, K_{22} and K_{33} are the splay, twist and bend elastic constants. Using the values of elastic constants from reference [21], the bare elastic constant L is estimated to be $\sim 3 \times 10^{-13}$ J/cm. The estimated bare coherence length $\xi_0 \sim 10$Å. Using these parameters numerically $S(z)$ profile for half the cell thickness at a few temperatures in the nematic phase are calculated. The variation of calculated $S(z)$ for half cell thickness at $T_{NI} - 5^0$ and $T_{NI} - 1^0$ as a function of z/ξ_0 are shown (continuous line) in Figure 4.48. It may be noted that the surface order parameter decays to a value hardly different from S_m when $z/\xi_0 \sim 50$. The thickness averaged order parameter in the cell is calculated by integrating $S(z)$,

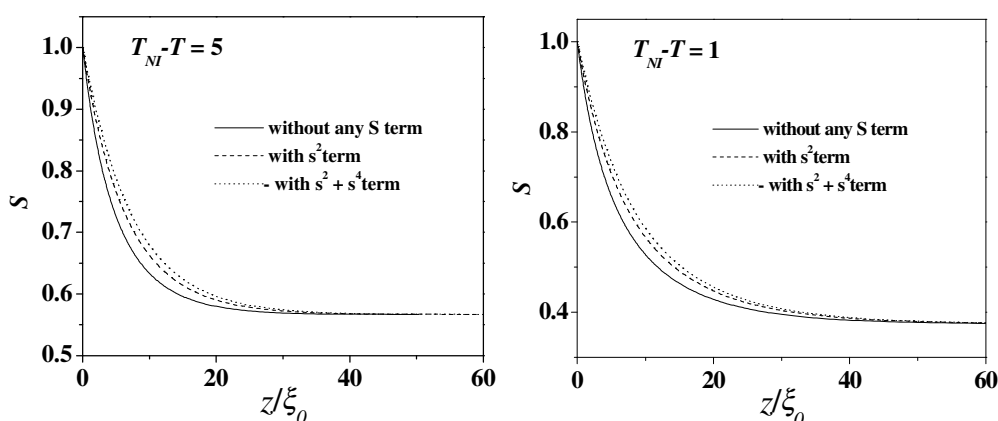$$\bar{S} = \frac{1}{t}\int_{0}^{t} S(z) \; dz \qquad 4.37$$

Figure 4.48: Variations of the calculated order parameter $S(z)$ (continuous line), $S_1(z)$ (dashed line) and $S_2(z)$ (dotted line) as functions of z/ξ_0 for half-cell thickness in the thin cell for temperature $T_{NI} - T = 5\ ^0$C and $1\ ^0$C. Variations are shown only up to z/ξ_0 = 60 for clarity. 1 μm corresponds to $z/\xi_0 = 1000$.

Dhara et al [17] also introduced an additional elastic term $L'\left[S\dfrac{dS}{dz}\right]^2$ in equation 4.26 where L' is also an elastic constant. This term is allowed by the symmetry of the medium. Following a procedure similar to that given above and assuming $L = L'$, we find

$$\frac{z}{\xi_0} = \int_{s(z)}^{1} \sqrt{\frac{1+S^2}{F(S)-F(S_m)}}\ dS \qquad\qquad 4.38$$

Assuming the same material parameters α, B, C, T^* numerically $S_1(z)$ profile for half the cell thickness using equation 4.38 at a few temperatures in the nematic phase are calculated. The suffix 1 indicates that an additional elastic term is used. Two such profiles at $T_{NI} - 5^0$ and $T_{NI} - 1^0$ are shown as a function of z/ξ_0 (dashed line) in Figure 4.48. It may be noted that the over all variation of $S_1(z)$ is similar to that of $S(z)$. The order parameter $S_1(z)$ is somewhat higher between $z/\xi_0 = 0$ to 50 than that of $S(z)$.

Order electricity is an electric polarization arising due to the gradient in the magnitude of order parameter S [22]. The associated polarization $P_o = r_1(n.\nabla s)n + r_2\nabla s$, creates a depolarizing field E_o. The coefficients r_1 and r_2 are proportional to S^2 [22]. At a planar interface, the interfacial order electric depolarization energy is given by $\dfrac{1}{2}(4\pi/\varepsilon)P_o^2$. The contribution due to order-electric polarization will be prominent in *thin* cells as the order parameter profile varies drastically near the boundaries (see Figure 4.48). We write the additional term arising due to this as $L''\left[S^2\dfrac{dS}{dz}\right]^2$ where L'' has the dimension of an elastic constant. The LdG free energy can be written as

$$\varphi = f(S) + L\left[\frac{dS}{dz}\right]^2 + L'S^2\left[\frac{dS}{dz}\right]^2 + L''S^4\left[\frac{dS}{dz}\right]^2 \qquad\qquad 4.39$$

Following a similar procedure as described above and assuming $L = L' = L''$ for simplicity, we find

$$\frac{z}{\xi_0} = \int_{s(z)}^{1} \sqrt{\frac{1 + S^2 + S^4}{F(S) - F(S_m)}} \; dS \qquad\qquad 4.40$$

Again assuming the same material parameters α, B, C, T^* numerically the $S_2(z)$ profile at a few temperatures are calculated, where the suffix 2 indicates that two elastic additional terms are used. The calculated order parameter profile $S_2(z)$ using at temperatures $T_{NI} - 5^0$ and $T_{NI} - 1^0$ are shown by dotted line in Figure 4.48. It can be noticed that the over all variation of $S_2(z)$ is similar to that of $S(z)$, with the value of the former being higher than that of the latter between $z/\xi_0 = 0$ to 50.

The thickness averaged order parameters $\overline{S}_1$ and $\overline{S}_2$ in the cell are calculated by integrating $S_1(z)$ and $S_2(z)$ respectively in place of $S(z)$ in equation 4.37. In Table 2 we give the calculated values of the order parameter in the bulk S_b, obtained from equation 4.25. Also the values of $\overline{S}$, $\overline{S}_1$ and $\overline{S}_2$ in the 1μm cell at a few temperatures are given in Table 2.

$T_{NI} - T$ (in ^{0}C)	S_b	$\overline{S}$	$\overline{S}_1$	$\overline{S}_2$	$\dfrac{\overline{S} - S_b}{S_b} \times 100$	$\dfrac{\overline{S}_1 - S_b}{S_b} \times 100$	$\dfrac{\overline{S}_2 - S_b}{S_b} \times 100$
0.2	0.297	0.310	0.313	0.314	4.4%	5.4%	5.7%
1	0.374	0.383	0.385	0.386	2.4%	2.9%	3.2%
5	0.566	0.571	0.572	0.573	0.9%	1.1%	1.2%
10	0.715	0.717	0.718	0.719	0.3%	0.4%	0.6%

Table 2: The values of bulk order parameter S_b and the average order parameters $\overline{S}$, $\overline{S}_1$ and $\overline{S}_2$ in the 1μm cell at a few temperatures below T_{NI} and the percentage enhancement in the average order parameters in 1μm thin cell compared to the bulk order parameter measured in a thick cell.

It may be noted that close to T_{NI} the enhancement is large and decreases rapidly as the temperature is lowered. This trend is expected as the perfect order at the

surface has a large effect when the bulk order parameter is lower. The bulk order parameter is increased with decreasing temperature and the effect of surface order is reduced. It can also be noticed that the enhancement of S at lower temperatures is comparatively larger for $\bar{S}_2$.

On the other hand, experimentally, we find that the enhancement of order parameter increases at lower temperatures (see Figure 4.35).

The enhancement of order parameter due to the reduction of the cell thickness has two aspects as discussed above. Firstly, the number of fluctuation modes are reduced (see section 4.41). This increases the order parameter by ~0.1% when the thickness is decreased from 10μm to 1μm. Secondly with a strong surface ordering potential, the thickness averaged value of order parameter $\bar{S}$ in thin cells is enhanced. As $K \propto S_0^2$, increased value of $\bar{S}$ in turn leads to an increase in the effective curvature elastic constant K, which results in a reduction in the *fluctuation amplitude* [17] (see equation 4.24). To estimate this effect we simply use the average values $\bar{S}_1$ and $\bar{S}_2$ in place of S_0 in equation 4.24 and use $\bar{K} = K_0 (\bar{S}_1)^2$, $\bar{K} = K_0 (\bar{S}_2)^2$ respectively to calculate S_{meas}. In this calculation we use $K_0 = 2 \times 10^{-6}$ dynes and $a = 20$ Å. The calculated values of S_{meas} in cells of thicknesses 10 μm and 1 μm at a few temperatures are also shown in Table 3.

$T_{NI} - T$ (in ^{0}C)	S_{meas}(1μm) (using $\bar{S}_1$)	S_{meas}(1μm) (using $\bar{S}_2$)	S_{meas}(10μm)	$\dfrac{S_{meas}(1\mu m) - S_{meas}(10\mu m)}{S_{meas}(10\mu m)} \times 100$ (using $\bar{S}_1$)	$\dfrac{S_{meas}(1\mu m) - S_{meas}(10\mu m)}{S_{meas}(10\mu m)} \times 100$ (using $\bar{S}_2$)
0.2	0.119	0.120	0.092	29.3%	30.4%
1	0.227	0.229	0.210	8.1%	9.0%
5	0.468	0.469	0.460	1.7%	2.0%
10	0.636	0.637	0.632	0.6%	0.8%

Table 3: Calculated values of S_{meas} using equation 4.22 with S_0 replaced by $\bar{S}_1$ and $\bar{S}_2$ respectively at a few temperatures.

The value of S_{meas} is less than the mean field order parameter S_0 due to the director fluctuations in both 10 μm and 1 μm thick cells. However the relative

enhancement of S_{meas} in a cell of thickness 1 μm is larger than that of $\bar{S}_1$ and $\bar{S}_2$. Thus the combined effect of the surface potential and the stiffening of the elastic constant has amplified the enhancement of S_{meas}. The enhancement is very large near the transition point and again decreases sharply as the temperature is lowered. On the other hand, the experimentally measured enhancement remains high as the temperature is lowered in the nematic phase (Figure 4.35). The calculated enhancement in S_{meas} is comparatively larger by using $\bar{S}_2$ than that using $\bar{S}_1$ at lower temperatures. However, the enhancement observed experimentally well below T_{NI} is much larger than the calculated value.

The order parameter coherence length $\xi_0 = \sqrt{\dfrac{L}{\alpha T_{NI}}}$, and the Landau co-efficient α can be determined using either the latent heat data or using the magnetic birefringence data (the Cotton-Mouton effect). The latent heat data available in the literature using adiabatic calorimetry technique is ~ 0.4 – 0.6KJ/g [23]. The value of α calculated using the latent heat is ~ 0.1 J/cm^3-K The Cotton-Mouton co-efficient is defined as $\kappa = \dfrac{\Delta\mu_{ind}}{H^2} = \dfrac{\Delta\chi_0 \Delta\mu_0}{3\alpha(T-T*)}$, where $\Delta\mu_{ind}$ is the induced birefringence due to magnetic field, H is the value of applied magnetic field strength. $\Delta\chi_0$ and $\Delta\mu_0$ are the diamagnetic susceptibility anisotropy and birefringence in the fully aligned nematic phase respectively. Bradshaw et al [24] have measured the diamagnetic susceptibility as a function of temperature and Bunning et al [25] have measured the temperature variations of birefringence for the n-alkyl-cyanobiphenyls and n-alkoxy-cyanobiphenyls (for n = 5 to 8). We have estimated the $\Delta\chi_0$ and $\Delta\mu_0$ values using Haller's extrapolation. The induced magnetic birefringence data on these compounds were reported by Muta et al [26]. Using these data we have estimated the Landau coefficient α and found that it can have values from ~ 0.1 J/cm^3-K to ~ 0.25 J/cm^3-K for different compounds. Another parameter is L, the bare elastic constant, whose value is found to be robust experimentally. Hence with this set of parameters we cannot explain the experimentally observed enhancement in the order parameter.

If we treat $\xi_0 \simeq a$ as an adjustable parameter then we get a better theoretical estimate of the enhancement for ξ_0=100Å and $q=2\pi/a$, as shown in Table 4.

$T_{NI}-T$ (in ^{0}C)	S_b	$\bar{S}$	$\bar{S}_1$	$\bar{S}_2$	$\dfrac{\bar{S}-S_b}{S_b}\times100$	$\dfrac{\bar{S}_1-S_b}{S_b}\times100$	$\dfrac{\bar{S}_2-S_b}{S_b}\times100$
0.2	0.297	0.374	0.451	0.461	25.9%	51.8%	55.2%
1	0.374	0.430	0.487	0.496	15.0%	30.2%	33.0%
5	0.566	0.596	0.624	0.631	5.3%	10.2%	11.5%
10	0.715	0.731	0.747	0.752	2.2%	4.5%	5.2%

Table 4: The values of bulk order parameter S_b and the average order parameters $\bar{S}$, $\bar{S}_1$ and $\bar{S}_2$ (using ξ_0=100Å) in the 1μm cell at a few temperatures below T_{NI}. The percentage enhancement in the average order parameters in 1μm cell compared to the bulk order parameter measured in thick cell.

It can be observed from Table 4 that assuming the value of bare correlation length ξ_0 =100Å, the enhancement of order parameter at lower temperatures is improved and is of the order of experimentally observed values. However, the physical basis for such a large value of ξ_0 is not clear. At temperatures nearer the transition point the estimated enhancement is very large and is connected with the assumption that the order parameter at the surface is saturated.

Thus, the Landau de Gennes theory for the uniaxial medium only partially accounts for the enhancement of the order parameter if the surface potential produces perfect order. Both the number of fluctuation modes as well as the fluctuation amplitude are reduced in thin cells. The latter effect is due to the stiffening of the elastic constant because of the enhanced order and has a significant influence on the *measured* order parameter. However the calculated values of the enhancement of order parameter decrease sharply as the temperature is lowered from T_{NI}. On the other hand in our experiments the enhancement actually *increases* at lower temperatures.

The limitation of LdG theory is that it is a mean field theory which is valid near the NI transition point. We are using this theory at very low temperatures deep in the nematic medium, where the theory is not expected to give reasonable results. Thus, the measured enhancement clearly points to the inadequacy of the theoretical approaches.

4.5 Discussion

In *planar* aligned cells the increase of nematic-nematic transition temperature with decreasing thickness of the cell (see Figure 4.44) appears to be associated with the enhancement of order parameter in thin cells compared to that in thick cells (Figure 4.35). However, LdG theory (see previous section) cannot fully account for the experimentally observed enhancement of order parameter in thin cells at lower temperatures as it is a mean field theory valid only near the NI transition temperature.

Our motivation to carry out experimental studies on the above binary mixture was to get a system exhibiting the N_1N_d transition in a convenient temperature range at atmospheric pressure. But the results of our X-ray study on the binary mixture with 60 mol% of CP6B indicate that there is no N_1 type of short range order in the nematic medium at lower temperatures. The *constant* value of layer spacing d (~26.3 Å) of short range ordered groups observed throughout the nematic range indicates that antiparallel association between the molecules is favoured at *all* temperatures. And also the temperature variation of dielectric constant $\varepsilon_{\parallel}$ is smooth throughout the entire nematic range (Figures 4.20-4.21) and does not exhibit an additional enhancement at lower temperatures which would have reflected a polar short range order. As discussed in chapter 3 in pure CP7B the N_1N_d transition takes place at high densities. Basappa et al [27] have also observed that the slope of the temperature dependence of $\varepsilon_{\parallel}$ increases by a small amount around T_{NN} in a 10 μm cell of CP7B subjected to a field of 600 esu. But in the mixture studied by us, it is possible that the number density is *not high enough* for the short range order to switch over to the polar 'monolayer' type. As discussed in chapter 3 the electrostatic interaction between the strongly dipolar cyano groups of neighbouring molecules favours an antiparallel orientation between them at modest densities [28]. The aromatic cores of the molecules have large polarizabilities and the strong dispersion interaction between such cores of neighbouring molecules leads to an antiparallel association between the molecules. Neighbouring molecules in the mixture can form pairs with antiparallel configuration of three different types, viz. LL, SS and LS as shown in Figure 4.49. (a) In LL , a molecule with the longer aromatic core (4PCPP) forms a pair with another 4PCPP molecule, (b) In SS, a molecule with the shorter aromatic core

(CP6B) forms a pair with another CP6B molecule, (c) In LS, a 4PCPP molecule forms a pair with a CP6B molecule.

The London dispersion interaction energy between the two molecules is given by $E \sim -h\overline{v}\alpha_1\alpha_2 / r^6$, where α_1 and α_2 are the polarisabilities of the two molecules, r is the intermolecular separation, h the plank constant and $\overline{v}$ an average absorption frequency. Assuming that the polarisabilities are proportional to the number of aromatic rings, the interaction energies for the three types of pairs LL, SS and LS will be in the ratio of 9:4:6.

(a) LL   **(b) SS**   **(c) SL**
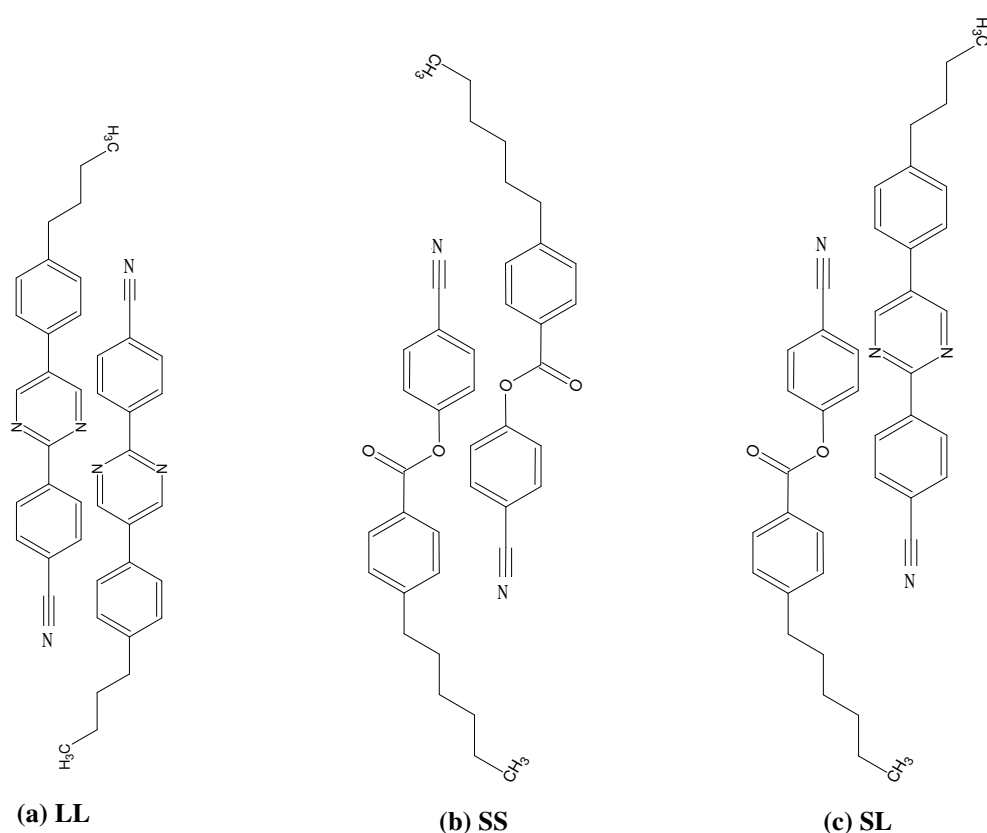
Figure 4.49: Schematic representation of intermolecular antiparallel associations of neighbouring molecules. L and S represent the molecules with longer aromatic core and shorter aromatic core respectively.

At *high* temperatures all the three different configurations are entropically favoured. It is expected that at *low* temperatures only two types of antiparallel associations between molecules viz., LL and SS in which a molecule forms a pair with its own kind are energetically favoured. Indeed by breaking up two SL pairs to

from an LL and an SS pair, the energy is lowered by ~ 8%. Hence we speculate that the NN transition observed in this binary mixture is associated with a change in short range order in which the high temperature phase (N_h) consists of antiparallel pairs of all the three kinds (LL, SS and LS) and goes over to a nematic (N_l) with predominantly two types of antiparallel associations (LL and SS) at low temperatures. This is a *new* type of NN transition which has not been predicted by theoretical models. It is clear that this change in the short range order *does not change* the average layer spacing *d* of the short range ordered groups.

As mentioned in section 4.32 in *planar* aligned cells a surface transition takes place before the bulk NI transition. The planar aligned cells are prepared using polyimide which is aromatic in nature. Indeed, experiments by Dhara et al [17] show that molecules with large aromatic cores have a large affinity towards the rubbed polyimide surface. Hence it is possible that the number density of 4PCPP with the longer aromatic core is relatively large at the surface. At low temperatures the concentration of LL type of short range ordered groups can grow larger near the surfaces. This effect is more pronounced in thinner cells, and the N_lN_h transition appears as a first order transition in thin cells (Figures 4.27, 4.28, 4.30, 4.31). The strength of first order transition decreases with increasing cell thickness and approaches a critical point at a finite thickness (see section 4.32). This type of NN transition between two uniaxial nematics with a change in such a type of short range order has been observed for the *first time*.

ODSE, an amphiphilic molecule used in the preparation of homeotropically aligned cells has 18 carbon atom chains. The interaction of the flexible chains of the molecules with the ODSE chains favours homeotropic alignment. Hence CP6B, with a somewhat longer chain with 6 carbon atoms has a better affinity towards the surface than 4PCPP with a 4 carbon atom chain. The N_lN_h transition in this geometry is independent of thickness of the cell (Figure 4.11) indicating that the effect of the aligning surface is not very prominent in this geometry. Probably the order parameter of the nematic is not enhanced much by the ODSE coated surface. The strong scattering of light observed in planar aligned thick cells (Figures 4.32, 4.33) as well as homeotropically aligned cells (Figures 4.6-4.12) indicate that this transition occurs very close to a critical point, at which a rapid change in short range ordering of the

molecules of the above mentioned type takes place. Even the two different activation energies obtained using dielectric relaxation studies (see section 4.312) in the different temperature ranges is also a reflection of the change in short range ordering of groups of molecules. This type of transition is possible only in mixtures with different types of molecules and *not* in pure compounds. Hence we believe that this is a new type of NN transition and more detailed studies on this system are necessary for a better elucidation of the nature of the short range order. We plan to take up some more experimental studies in the near future.

4.6   Conclusions

We have observed a *new* type of NN transition in <u>binary mixtures</u> made of highly polar molecules viz., 4PCPP, with a longer aromatic core and CP6B with a shorter aromatic core. We believe that the high temperature nematic phase is characterised by three types of antiparallel pairs of molecules viz., two types of pairs formed out of same type of molecules and the other pair formed out of the two different species. At low temperatures the antiparallel pairs of molecules formed out of two different species are *not* favoured. In *homeotropically* aligned cells the NN transition temperature is *independent* of thickness of the cell. In *planar* aligned cells the increase in NN transition temperature with decreasing thickness of the cell appears to be associated with the enhancement of the order parameter in thin cells. Critical slowing down of director fluctuations observed in homeotropically aligned geometry indicate that the system is close to the *critical* point.

References

1. P. G. de Gennes and J. Prost, *The Physics of Liquid Crystals*, Clarendon Press, Oxford, 1993.

2. G. Basappa and N.V. Madhusudana, "Effect of strong electric fields on phase transitions in some liquid crystals", *Mol. Cryst. Liq. Cryst.* **288**, 161-174, 1996.

3. J. Prost and J. Toner, "Dislocation-loop melting theory of phase diagrams with nematic regions surrounded by smectic regions", *Phys. Rev. A* **36**, 5008-5014, 1987.

4. V.V. Titov, E.I. Kovshev, A.I. Pavluchenko, V.T. Lazareva and M.F. Grebenkin, "Synthesis and properties of nematic liquid crystals exhibiting a positive dielectric anisotropy", *J.de. Physique*. **36C1**, 387-392, 1975.

5. L. M. Blinov, "Electro-optical and magneto-optical properties of liquid crystals", *Wiley –Interscience Publication* (John Wiley & Sons Limited), p63, 1983.

6. B. R. Ratna and R. Shashidhar, "Dielectric Dispersion in 4′-n-Alkyl-4-Cyanobiphenyls", *Mol. Cryst. Liq. Cryst.* **42**, 185-192, 1977.

7. H. Kresse, "Dynamic dielectric properties of nematics", section **6.2** in *Physical Properties of Liquid crystals: Nematics,* Ed.by D.A. Dunmur, A. Fukuda and G.R. Luckhurst, INSPEC publication, 277-287, 2001.

8. G. Meier and A. Saupe, "Dielectric Relaxation in Nematic liquid crystals", *Mol. Cryst.* **1**, 515-525, 1966; A. J. Martin, G. Meier and A. Saupe, Symp. Fararday Soc. **5**, 119, 1971.

9. W. H. de Jeu and Th. W. Lathouwers, "Nematic Phenyl Benzoates in Electric Fields I. Static and Dynamic Properties of the Dielectric Permittivity", *Mol. Cryst. Liq. Cryst.* **26**, 225-234, 1973.

10. L. Benguigui, "Dielectric relaxation in liquid crystals", *Mol. Cryst. Liq. Cryst.,* **114**, 51-63, 1984.

11. A.C. Diogo and A.F. Martins, "Thermal behaviour of the twist viscosity in a series of homologous nematic liquid crystals", *Mol. Cryst. Liq. Cryst.* **66**, 133-146, 1981.

12. B. Jha, A. Nandi, S. Paul and R. Paul, "Orientational Distribution Function and Order Parameters for 5-(4-n-Butylphenyl)-2-(4-cyanophenyl)-Pyrimidine", *Mol. Cryst. Liq. Cryst.* **104**, 289-300, 1984.

13. P. Sheng, "Boundary-layer phase transition in nematic liquid crystals", *Phys. Rev. A* **26**, 1610-1617, 1982.

14. P. Sheng, "Phase transition in surface-aligned nematic films", *Phys. Rev. Lett.* **37**, 1059-1062, 1976.

15. H. Mada and S. Kobayashi, "Surface and bulk order parameter of a nematic liquid crystal", *Appl. Phys. Lett.* **35** (1), 4-5, 1979; H. Mada and S. Kobayashi, "Wavelength and voltage dependances of refractive indices of nematic liquid crystals", *Mol. Cryst. Liq. Cryst.* **33**, 47-53, 1976.

16. Sobha R Warrier, D. Vijayaraghavan and N.V. Madhusudana, "Evidence for a nematic-nematic transition in thin cells of a highly polar compound", *Europhys. Lett.* **44**, 296-301, 1998.

17. Surajit Dhara and N.V. Madhusudana, "Enhancement of orientational order parameter of nematic liquid crystals in thin Cells", *Eur. Phys. J.E.* **13**, 401- 408, 2004.

18. D. A. Dunmur and K. Szumilin "Field quenching of director fluctuations in thin films of nematic liquid crystals", *Liq. Cryst.* **6**, 449- 455, 1989.

19. J. V. Selinger and D. R. Nelson, "Density functional theory of nematic and smectic-A order near surfaces", *Phys. Rev. A* **37**, 1736-1746, 1988.

20. E. F. Gramsbergen, L. Longa and W. H. de Jeu, "Landau theory of the nematic-isotropic phase transition", *Phys. Rep.* **135**, 195-257, 1986.

21. U. Finkenzeller, T. Geelhaar, G. Weber and L. Pohl, "Liquid crystalline reference compounds", *Liq. Cryst.* **5**, 313-321, 1989.

22. G. Durand, "Order electricity in liquid crystals", *Physica A* **163**, 94-100, 1990; G. Barbero, I. Dozov, J.F. Palierne and G.Durand , "Order Electricity and Surface Orientation in Nematic Liquid Crystals", *Phys. Rev. Lett*. **56**, 2056-2059, 1986.

23. M. Sorai, "Calorimetric measurements in nematics", section **3.2** in *Physical Properties of Liquid crystals: Nematics,* Ed.by D.A. Dunmur, A. Fukuda and G.R. Luckhurst, INSPEC publication, 141-150, 2001.

24. M.J. Bradshaw, E.P. Raynes, J.D. Bunning and T.E. Faber, "The Frank constants of some nematic liquid crystals", *J. Physique* **46**, 1513-1520, 1985.

25. J.D. Bunning, D.A. Crellin and T.E. Faber, "The effect of molecular biaxiality on the bulk properties of some nematic liquid crystals", *Liq. Cryst.* **1**, 37-51, 1986.

26. K. Muta, H. Takezoe, A. Fukuda and E. Kuze, "Cotton-Mouton Effect of Alkyl and Alkoxy – Cyanobiphenyls in Isotropic phase", *Jpn. Journ. of Appl. Phys.* **18**, 2073-2080, 1979.

27. G. Basappa and N.V. Madhusudana, "Effect of a strong electric field on a nematogen: evidence for polar short range order", *Eur. Phys. J. B* **1**, 179-187, 1998; G. Basappa, "Experimental studies on the relationship between order and physical properties in liquid crystals", *Ph.D. Thesis*, Mysore University, 1997.

28. N.V. Madhusudana and S. Chandrasekhar, "The role of permanent dipoles in nematic order", *Pramana* (*Suppl*.) **1**, 57-68, 1975.